



**HAL**  
open science

## Quantitative magnetization transfer MRI unbiased by on-resonance saturation and dipolar order contributions

Lucas Soustelle, Thomas Troalen, Andreea Hertanu, Jean-philippe Ranjeva, Maxime Guye, Gopal Varma, David C Alsop, Guillaume Duhamel, Olivier M Girard

### ► To cite this version:

Lucas Soustelle, Thomas Troalen, Andreea Hertanu, Jean-philippe Ranjeva, Maxime Guye, et al.. Quantitative magnetization transfer MRI unbiased by on-resonance saturation and dipolar order contributions. *Magnetic Resonance in Medicine*, 2023, 10.1002/mrm.29678 . hal-04103313

**HAL Id: hal-04103313**

**<https://amu.hal.science/hal-04103313>**

Submitted on 23 May 2023

**HAL** is a multi-disciplinary open access archive for the deposit and dissemination of scientific research documents, whether they are published or not. The documents may come from teaching and research institutions in France or abroad, or from public or private research centers.

L'archive ouverte pluridisciplinaire **HAL**, est destinée au dépôt et à la diffusion de documents scientifiques de niveau recherche, publiés ou non, émanant des établissements d'enseignement et de recherche français ou étrangers, des laboratoires publics ou privés.



Distributed under a Creative Commons Attribution 4.0 International License

# Quantitative magnetization transfer MRI unbiased by on-resonance saturation and dipolar order contributions

Lucas Soustelle<sup>1,2</sup>   | Thomas Troalen<sup>3</sup>  | Andreea Hertanu<sup>1,2</sup>  |  
Jean-Philippe Ranjeva<sup>1,2</sup>  | Maxime Guye<sup>1,2</sup>  | Gopal Varma<sup>4</sup>  |  
David C. Alsop<sup>4</sup>  | Guillaume Duhamel<sup>1,2</sup>  | Olivier M. Girard<sup>1,2</sup> 

<sup>1</sup>Aix Marseille Univ, CNRS, CRMBM, Marseille, France

<sup>2</sup>APHM, Hôpital Universitaire Timone, CEMEREM, Marseille, France

<sup>3</sup>Siemens Healthcare SAS, Courbevoie, France

<sup>4</sup>Division of MR Research, Department of Radiology, Beth Israel Deaconess Medical Center, Harvard Medical School, Boston, Massachusetts, USA

## Correspondence

Lucas Soustelle, Centre de Résonance Magnétique Biologique et Médicale, Aix Marseille Université, CRMBM UMR 7339 – Faculté de Médecine, 27 Boulevard Jean Moulin, 13005 Marseille, France.  
Email: [lucas.soustelle@univ-amu.fr](mailto:lucas.soustelle@univ-amu.fr)

## Funding information

Agence Nationale de la Recherche, Grant/Award Numbers: ANR-22-CE17-0060, ANR-22-CE18-0041, ANR-17-CE18-0030, ANR-11-INBS-0006; ARSEP, Grant/Award Number: ARSEP 2020

**Purpose:** To demonstrate the bias in quantitative MT (qMT) measures introduced by the presence of dipolar order and on-resonance saturation (ONRS) effects using magnetization transfer (MT) spoiled gradient-recalled (SPGR) acquisitions, and propose changes to the acquisition and analysis strategies to remove these biases.

**Methods:** The proposed framework consists of SPGR sequences prepared with simultaneous dual-offset frequency-saturation pulses to cancel out dipolar order and associated relaxation ( $T_{1D}$ ) effects in Z-spectrum acquisitions, and a matched quantitative MT (qMT) mathematical model that includes ONRS effects of readout pulses. Variable flip angle and MT data were fitted jointly to simultaneously estimate qMT parameters (macromolecular proton fraction [MPF],  $T_{2,f}$ ,  $T_{2,b}$ , R, and free pool  $T_1$ ). This framework is compared with standard qMT and investigated in terms of reproducibility, and then further developed to follow a joint single-point qMT methodology for combined estimation of MPF and  $T_1$ .

**Results:** Bland–Altman analyses demonstrated a systematic underestimation of MPF (−2.5% and −1.3%, on average, in white and gray matter, respectively) and overestimation of  $T_1$  (47.1 ms and 38.6 ms, on average, in white and gray matter, respectively) if both ONRS and dipolar order effects are ignored. Reproducibility of the proposed framework is excellent ( $\Delta$ MPF = −0.03% and  $\Delta$  $T_1$  = −19.0 ms). The single-point methodology yielded consistent MPF and  $T_1$  values with respective maximum relative average bias of −0.15% and −3.5 ms found in white matter.

**Conclusion:** The influence of acquisition strategy and matched mathematical model with regard to ONRS and dipolar order effects in qMT-SPGR frameworks has been investigated. The proposed framework holds promise for improved accuracy with reproducibility.

## KEYWORDS

dipolar order, inhomogeneous magnetization transfer, neuroimaging, quantitative magnetization transfer,  $T_1$  relaxometry

This is an open access article under the terms of the [Creative Commons Attribution](https://creativecommons.org/licenses/by/4.0/) License, which permits use, distribution and reproduction in any medium, provided the original work is properly cited.

© 2023 The Authors. *Magnetic Resonance in Medicine* published by Wiley Periodicals LLC on behalf of International Society for Magnetic Resonance in Medicine.

## 1 | INTRODUCTION

Quantitative magnetization transfer (qMT) imaging aims at quantitatively assessing the magnetization exchange processes occurring between motion-restricted macromolecules and surrounding water protons. For brain imaging, the classical qMT methodology uses a two-pool model<sup>1–3</sup> applied to MT-prepared spoiled gradient-recalled (SPGR) data.<sup>4</sup> The most relevant quantitative parameter derived from this approach is the macromolecular proton fraction (MPF), which presents a fair sensitivity to brain tissue changes.<sup>5,6</sup> In the qMT framework, an independent measurement of  $T_1$  relaxation is required to disentangle relaxation and MT effects, and provide access to an estimation of MPF. Variable flip angle (VFA)–SPGR and MT-SPGR data are usually combined and either used separately<sup>7–9</sup> or jointly<sup>10</sup> to estimate the apparent free pool  $T_1$  and other qMT parameters. The joint estimation is advantageous, as it explicitly considers magnetization exchanges between the macromolecular and the free pools in the two-pool model for a more accurate  $T_1$  and MPF estimation.<sup>11</sup>

However, two important features are typically not considered in common SPGR-based qMT methodology:

- First, on-resonance saturation effects induced by the readout pulses on the macromolecular lineshape are usually ignored. Of interest, Mossahebi et al.<sup>10</sup> have argued that on-resonance saturation effects of the SPGR readout pulse at the macromolecular pool level may have a nonnegligible effect on the qMT parameters' estimation. This was further demonstrated by ensuing work in the context of magnetic resonance fingerprinting<sup>12</sup> and VFA- $T_1$  mapping.<sup>13,14</sup> It is therefore worth investigating whether these saturation effects (referred hereafter to as on-resonance saturation [ONRS]) may bias the estimated values of qMT parameters if not accounted for in the joint VFA-SPGR and MT-SPGR data modeling.
- Second, the off-resonance RF saturation of the semisolid pool should be treated using the Provotorov theory,<sup>15,16</sup> which demonstrates a coupling between the macromolecular Zeeman and dipolar orders when applying single-offset RF irradiation. Early studies concluded a negligible effect from dipolar order in the estimation of the qMT parameter values<sup>17,18</sup> from single-offset frequency saturation (SOFS; RF irradiation applied at a single side with respect to the resonance frequency) Z-spectrum data. Hence, it was argued that the classical binary spin-bath model—which neglects dipolar order contributions—was appropriate for the modeling of SOFS-based qMT data. However, these early experiments were performed either on agar gel

phantoms, which are not representative of the brain tissue and have weak dipolar order effects,<sup>18</sup> or on ex vivo white matter samples at room temperature,<sup>17</sup> which strongly limits the influence of dipolar order on the macromolecular magnetization.<sup>19–21</sup> Recent investigations have shown that myelinated central nervous system tissues are associated with relatively strong dipolar order effects as denoted by a long dipolar order relaxation time ( $T_{1D}$ ;  $T_{1D} \approx 6–10$  ms) and as identified by inhomogeneous magnetization transfer (ihMT) imaging in studies with ex vivo (at physiological temperature) and in vivo specimens from animals, such as in mouse brains<sup>22–24</sup> and rat spinal cord,<sup>25</sup> and in humans brains.<sup>26–28</sup> Hence, and given the typical irradiation powers used in clinical MR scanners for pulsed SOFS qMT experiments, the conditions for dipolar order to contribute to the MT signal in in vivo central nervous system tissues can be satisfied.<sup>29</sup> Because dipolar order effects manifest as a reduced RF saturation rate of the macromolecular pool,<sup>28</sup> which varies with the preparation pulse's power and frequency,<sup>21,25,30,31</sup> biases can be expected in the estimated qMT parameters from SOFS-based Z-spectra analyzed with the two-pool model. Conversely, an alternative approach involving symmetric dual-offset frequency saturation (DOFS; RF irradiation applied on both sides regarding the resonance frequency) pulses, which effectively decouples the dipolar orders from their associated macromolecular Zeeman orders,<sup>32,33</sup> would make the two-pool model more accurate for Z-spectrum data analyses.

In this work, qMT simulations and experiments were performed to confirm the existence of biases in quantitative MPF and longitudinal relaxation derived from SOFS-based Z-spectra analyzed with the classical two-pool model. Additionally, we propose an alternative framework based on DOFS pulses to cancel out dipolar order effects and a two-pool model that accounts for ONRS effects when deriving quantitative MT parameters from combined VFA-SPGR and MT-SPGR data in the human brain. The proposed framework was repeated for reproducibility assessment and further extended in an adapted joint single-point qMT methodology<sup>7</sup> for simultaneous estimation of MPF and apparent free pool  $T_1$ .

## 2 | METHODS

Experiments were performed on a 3T clinical scanner (MAGNETOM Vida, software version XA20A; Siemens Healthineers, Erlangen, Germany) with body coil transmission and a 32-channel receive head coil on 3 healthy

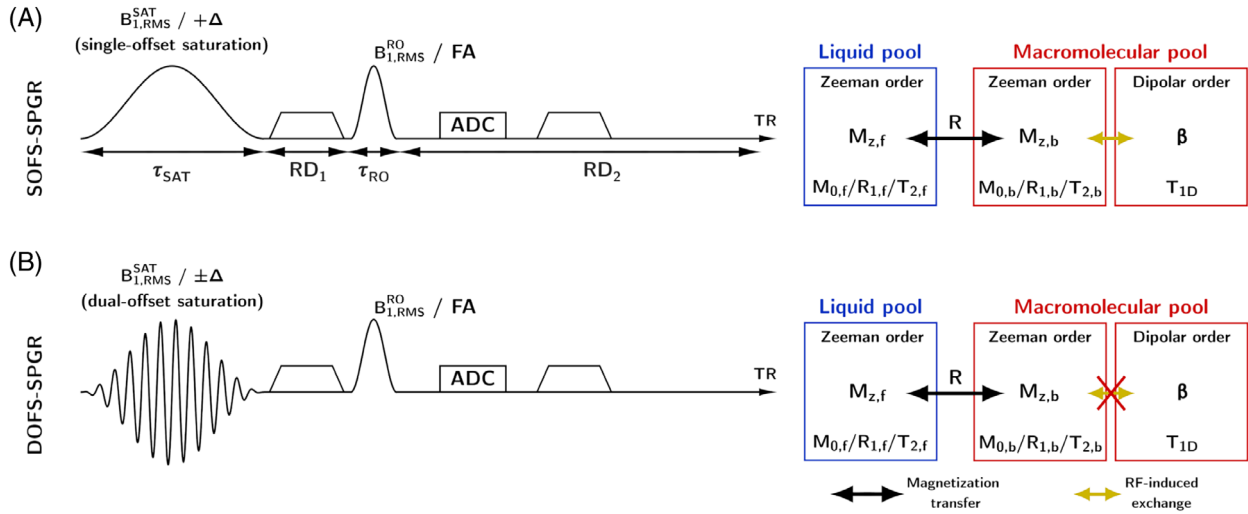


**FIGURE 1** Magnetization transfer (MT)-prepared spoiled gradient-recalled (SPGR) sequences with a single-offset ( $+\Delta$ ) saturation pulse (SOFS; RF irradiation applied at a single side with regard to the resonance frequency) (A), and with a simultaneous symmetric dual-offset ( $\pm\Delta$ ) saturation pulse (DOFS; RF irradiation applied at both sides regarding the resonance frequency) (B). The use of a simultaneous DOFS pulse effectively decouples the macromolecular Zeeman order from its associated dipolar order. Conversely, SOFS couples dipolar order and Zeeman order. The classical and commonly used two-pool quantitative MT (qMT) model, which does not include a dipolar order reservoir, is more accurately adapted to the DOFS-SPGR conditions.

volunteers (2:1 men:women; mean age:  $30.2 \pm 2.9$  years). Experiments were approved by the institutional ethics committee on clinical investigations (CRMBM, Marseille), and written informed consent was obtained from each participant before the study.

## 2.1 | Sequence description

Figure 1 shows the MT-prepared SPGR pulse sequences used in the experiments. The MT preparation includes either a SOFS (Figure 1A) or a DOFS (Figure 1B) pulse, both of identical duration  $\tau_{\text{SAT}}$ , followed by a spoiling gradient applied in the readout direction within a resting delay interval ( $\text{RD}_1$ ). The 3D-SPGR acquisition module includes a nonselective Hann-shaped readout pulse of duration  $\tau_{\text{RO}}$ , followed by a delay to TR ( $\text{RD}_2$ ), encompassing a gradient-echo readout and a spoiling gradient in the same direction as in the preparation.

SOFS pulses consisted of Hann-shaped pulses applied with off-resonance:

$$A^{\text{SOFS}}(t; \Delta) = A(t)e^{-2i\pi\Delta t} \quad (1)$$

Where  $\Delta$  is the pulse offset frequency from free water resonance, and  $A(t)$  its normalized amplitude, defined as follows:

$$A(t) = \frac{1}{2} \left( 1 - \cos\left(2\pi \frac{t - \tau_{\text{SAT}}}{\tau_{\text{SAT}}}\right) \right) \quad (2)$$

Simultaneous symmetric dual-offset saturation was achieved by modulating the SOFS pulse amplitude with a symmetric sine function, thereby guaranteeing that the on-resonance component (i.e., water) remains unaffected:

$$A^{\text{DOFS}}(t; \Delta) = A^{\text{SOFS}}(t; 0) \times \sin(2\pi\Delta(t - \tau_{\text{SAT}}/2)) \quad (3)$$

The saturation pulse power  $B_{1,\text{RMS}}^{\text{SAT}}$  is given by  $B_{1,\text{RMS}}^{\text{SAT}} = B_{1,\text{peak}}^{\text{SAT}} \sqrt{p_2^{\text{SAT}}}$ , where  $B_{1,\text{peak}}^{\text{SAT}}$  denotes the pulse peak  $B_1$  and  $p_2^{\text{SAT}}$  denotes the pulse power integral.<sup>34</sup> To apply equivalent saturation power, the  $B_{1,\text{peak}}^{\text{SAT}}$  of the DOFS pulses was increased by a  $\sqrt{2}$  factor to compensate for its halved power integral in comparison to that of the SOFS pulse.

In the following, and as classically modeled in qMT frameworks, we assume that RF irradiations are applied at an exact frequency offset  $\Delta$  despite originating from finite pulses characterized by a spectral response.

## 2.2 | Two-pool model for SPGR-based sequences

A two-pool model was adapted into a general matrix formalism accounting for magnetization saturation, tilting, relaxation, and exchange events throughout the MT-SPGR and VFA-SPGR sequences. The objective was to isolate the longitudinal magnetization of the free pool ( $M_{z,f}$ ) from the magnetization vector  $\mathbf{M} = [M_{x,f} \ M_{y,f} \ M_{z,f} \ M_{z,b}]^T$ .

The general cross-relaxation matrix was subsequently defined as follows:

$$\mathbf{A}_{\text{REX}} = \begin{bmatrix} -1/T_{2,f} & 0 & 0 & 0 \\ 0 & -1/T_{2,f} & 0 & 0 \\ 0 & 0 & -(R_{1,f} + RM_{0,b}) & RM_{0,f} \\ 0 & 0 & RM_{0,b} & -(R_{1,b} + RM_{0,f}) \end{bmatrix} \quad (4)$$

where  $M_{0,i}$ ,  $R_{1,i}$  ( $=1/T_{1,i}$ ) and  $T_{2,i}$  are the thermal equilibrium, longitudinal relaxation rate and transverse relaxation time of the free pool ( $i=f$ ) and macromolecular pool ( $i=b$ ), and  $R$  is the exchange rate between the two pools. The longitudinal relaxation times of both pools are assumed equal ( $T_{1,b} = T_{1,f} = T_1$ ), and we denote the resulting apparent relaxation time as  $T_1$  in the following. In addition, the convention  $M_{0,f} + M_{0,b} = 1$  was adopted, and MPF—defined as the ratio of the macromolecular magnetization over the total proton magnetization—then reduces to  $\text{MPF} = M_{0,b}$ .

The saturation matrix associated with the MT preparation pulse was defined as follows:

$$\mathbf{A}_{\text{SAT}} = \text{diag} \left( 0, 0, -W_f^{\text{SAT}}, -W_b^{\text{SAT}} \right) \quad (5)$$

where  $W_b^{\text{SAT}} = \pi g_b(\Delta, T_{2,b}) \times (\gamma B_{1,\text{RMS}}^{\text{SAT}})^2$  is the macromolecular saturation rate, using the super-Lorentzian absorption lineshape. This lineshape includes a residual broadening term as proposed by Pampel et al.,<sup>35</sup> an alternative to the extrapolation method for on-resonance saturation rate calculation.<sup>12,36</sup> The value of  $W_f^{\text{SAT}} = \pi g_f(\Delta, T_{2,f}) \times (\gamma B_{1,\text{RMS}}^{\text{SAT}})^2$  is the free pool saturation rate using a Lorentzian lineshape. Regarding the VFA-SPGR sequences, the terms  $W_b^{\text{SAT}}$  and  $W_f^{\text{SAT}}$  are set to 0.

In contrast, the rotation-saturation matrix corresponding to the on-resonance readout pulses was defined as follows, assuming a rotation about the  $x$ -axis, a constant pulse of duration  $\tau_{\text{RO}}$ , and no  $B_0$ -related deviation as the pulse duration is sufficiently short:

$$\mathbf{A}_{\text{RO}} = \begin{bmatrix} 0 & 0 & 0 & 0 \\ 0 & 0 & \text{FA}/\tau_{\text{RO}} & 0 \\ 0 & -\text{FA}/\tau_{\text{RO}} & 0 & 0 \\ 0 & 0 & 0 & -W_b^{\text{RO}} \end{bmatrix} \quad (6)$$

where  $W_b^{\text{RO}} = \pi g_b(\Delta = 0, T_{2,b}) \times (\gamma B_{1,\text{RMS}}^{\text{RO}})^2$  is the macromolecular saturation rate induced by the readout pulse, and  $\text{FA}$  (expressed in radians) and  $\tau_{\text{RO}}$  are the readout pulse flip angle and duration, respectively, and  $B_{1,\text{RMS}}^{\text{RO}}$  is the readout pulse  $B_{1,\text{RMS}}$ , as  $B_{1,\text{RMS}}^{\text{RO}} = B_{1,\text{peak}}^{\text{RO}} \sqrt{p_2^{\text{RO}}}$ .

The matrix formalism proposed by Malik et al.<sup>37</sup> was used to compute  $M_{z,f}$ 's amplitude in steady-state just before the readout pulse, assuming a perfect

spoiling condition and piecewise constant events. Each event-related matrix  $\mathbf{A}_i$  was rewritten as follows:

$$\tilde{\mathbf{A}}_i = \begin{bmatrix} \mathbf{A}_i & \mathbf{C} \\ 0 & \mathbf{C} \end{bmatrix} \quad (7)$$

where  $\mathbf{C} = [0 \ 0 \ R_{1,f}M_{0,f} \ R_{1,b}M_{0,b}]^T$  and “0” is a row vector of five “0” elements to match the matrix dimensionality.

The value of  $M_{z,f}$  was then calculated as the third eigenvector element associated with the eigenvalue equal to 1 of the  $\tilde{\mathbf{X}}$  matrix, defined as follows:

$$\tilde{\mathbf{X}} = e^{\tilde{\mathbf{A}}_{\text{REX}} \times \text{RD}_1} e^{(\tilde{\mathbf{A}}_{\text{SAT}} + \tilde{\mathbf{A}}_{\text{REX}}) \times \tau_{\text{SAT}}} e^{\tilde{\mathbf{A}}_{\text{REX}} \times \text{RD}_2} \Phi e^{(\tilde{\mathbf{A}}_{\text{RO}} + \tilde{\mathbf{A}}_{\text{REX}}) \times \tau_{\text{RO}}} \quad (8)$$

where  $\Phi = \text{diag}([0,0,1,1,1])$  ensures the transverse magnetization spoiling condition, and  $\text{RD}_1$  and  $\text{RD}_2$  refer to the resting delays after the saturation pulse and after the readout pulse, respectively (Figure 1). Finally, the transverse magnetization was computed as  $M_{xy,f} = M_{z,f} \times \sin(\text{FA})$ .

To eliminate the contribution of scaling factors including  $T_2^*$  decay, proton density, coil sensitivity profile and receiver gain, all signals were classically normalized by a reference obtained without saturation (referred hereafter to as  $\text{MT}_0$ ) for both simulations and experiments.

This two-pool model was used in simulations and experiments to estimate quantitative MT parameters according to different methodologies: (i) without considering ONRS effects ( $W_b^{\text{RO}} = 0$ ; model corresponds to the classical qMT model, hereafter referred to as qMT-noONRS) and (ii) considering ONRS effects ( $W_b^{\text{RO}} > 0$ ; hereafter referred to as qMT-ONRS).

### 2.3 | Simulations

Theoretical synthetic brain signals for VFA- and MT-SPGR sequences were generated with the same parameters used in the experiments (see Section 2.4) and using the Provotorov theory of RF saturation (Figure 1A), which accounts for the coupling between the Zeeman and dipolar orders of the macromolecular pool, as already described in the literature.<sup>25,32</sup> In practice, Eqs. (4)–(7) were modified to include the dipolar order contribution to the RF saturation ( $T_{1D}$  and RF-induced exchange rate with the Zeeman pool; see Appendix A) and applied for the generation of MT signals as a function of  $T_{1D}$  spanning from 10  $\mu\text{s}$  to 20 ms (hence mimicking an increasing contribution of dipolar order). Representative qMT parameters of white matter (WM) and gray matter (GM) were evaluated, with reference parameters ( $p_{\text{ref}}$ ;  $p = \{T_{2,f}, T_1, T_{2,b}, \text{MPF}, R\}$ ) set to  $T_{2,f} = 20/30$  ms,  $T_{2,b} = 11/10$   $\mu\text{s}$ ,  $T_1 = 1100/1600$  ms,  $\text{MPF} = 15.0/9.0\%$ , and  $R = 20/20$   $\text{s}^{-1}$ , respectively.<sup>38</sup> Simulations were performed for both SOFS and DOFS conditions, and the synthetic

signals were then fitted using the qMT-noONRS and qMT-ONRS mathematical models to estimate the qMT parameters ( $p_{est}$ ). The effects of dipolar order and ONRS on the estimation of qMT parameters were evaluated by computing the relative variation ( $RV_p$ ; expressed in %) between the estimated and reference parameters

$$RV_p = \frac{p_{est} - p_{ref}}{p_{ref}} \quad (9)$$

as well as the deviation of parameters ( $\Delta p = p_{est} - p_{ref}$ ; expressed in absolute units).

## 2.4 | MRI experiments

The imaging protocol consisted of 3D sagittal full Z-spectra and VFA acquisitions using the described MT-SPGR sequences (Figure 1). SOFS and DOFS-MT experiments were performed with the following MT pulse parameters: Hann-shaped pulse of duration  $\tau_{SAT} = 12.0$  ms, frequency offsets  $\Delta = 1/2/4/6/8/12/20$  kHz, RF saturation power  $B_{1,RMS}^{SAT} = 2.66/3.73$   $\mu$ T, and a readout pulse flip angle of  $10^\circ$ . VFA experiments were performed using the SOFS-SPGR sequence with the MT pulse's offset frequency tuned to 100 kHz (no MT effect at this frequency), to maintain a constant RF duty cycle. The sequence was run thrice with FA values of  $6^\circ$ ,  $10^\circ$ , and  $25^\circ$ . The  $MT_0$  reference image corresponded to the VFA image with FA =  $10^\circ$ . Common MT-SPGR and VFA-SPGR parameters were TR = 30.0 ms,  $RD_1 = 2.1$  ms, three monopolar gradient echoes at TE = 2.1/5.2/8.3 ms (advantageous for denoising purpose; see Section 2.5), Hann-shaped readout pulse of duration  $\tau_{RO} = 1.0$  ms, RF spoiling phase increment =  $50^\circ$ , readout bandwidth (BW) = 420 Hz/voxel, matrix size =  $128 \times 128 \times 72$  and voxel size = 2-mm isotropic, total gradient spoiling moment in the readout direction = 40 mT·ms/m after the MT pulse and post-echo readout, respectively, 5-s dummy scans, 6/8 partial Fourier in the phase direction, and  $2 \times 2$  CAIPIRINHA acceleration ( $24 \times 24$  integrated autocalibration lines); and acquisition time per volume = 1 min 23 s. SOFS and DOFS sequences paired with regard to  $\Delta$  and  $B_{1,RMS}^{SAT}$  values were run consecutively, and each pair was randomly distributed throughout the protocol. VFA acquisitions were randomly interleaved. An identical order was conserved for all subjects.

In addition, for segmentation purposes, a sagittal 3D  $T_1$ -weighted compressed-sensing MPRAGE sequence was acquired with the following parameters: TR/TE = 2300.0/2.9 ms, TI = 900.0 ms, BW = 240 Hz/voxel, readout FA =  $9^\circ$ , matrix size =  $256 \times 248 \times 176$ , and isotropic voxel size of 1 mm; and acquisition time = 1 min 57 s. A sagittal

interleaved and multislice  $B_1^+$  mapping sequence (constructor presaturated turbo-FLASH) was used with TR/TE = 26290.0/2.2 ms, BW = 490 Hz/voxel, saturation FA =  $80^\circ$ , readout FA =  $8^\circ$ , in-plane matrix size =  $96 \times 96$ , 60 slices, and reconstructed voxel size =  $3 \times 3 \times 3$  mm<sup>3</sup>; and acquisition time of 53 s.

The 3 subjects were scanned a second time after a 30-min break, using only the VFA and DOFS protocols for reproducibility assessment.

## 2.5 | Image processing

For each saturation protocol (i.e., SOFS and DOFS), the 51 SPGR images acquired per subject ( $[14 \{MT-SPGR\} + 3 \{VFA-SPGR\}] \times [3 \{TEs\}]$ ) were stacked together and denoised jointly using the Marchenko-Pastur principal component analysis routine from the *MRtrix3* package (v. RC301).<sup>39–41</sup> Each multi-echo SPGR image was then combined with a sum-of-squares operation to further enhance the SNR. Finally, VFA-weighted and MT-weighted (MTw) images were rigidly registered onto the respective VFA-SPGR image at FA =  $25^\circ$  to compensate for motion. The latter was rigidly registered onto the MPRAGE image, and the transformation and resampling operations were applied to all other SPGR images.

The qMT parameter values derived from qMT analyses were evaluated from regions of interest (ROIs) selected in WM and deep gray matter (DGM). For WM, ROIs were retrieved from the JHU probabilistic atlas<sup>42</sup> through label propagation of the MNI template (symmetric ICBM 2009c) onto the anatomical MPRAGE volume using a multistage, rigid, affine, and diffeomorphic registration (SyN<sup>43</sup>; *antsRegistrationSyN.sh*) implemented in the Advanced Normalization Tools (ANTs; v. 2.0.1<sup>44</sup>). DGM ROIs were automatically segmented using the *FreeSurfer* (v. 6.0.0) default *recon-all* pipeline on the MPRAGE image.<sup>45</sup>

### 2.5.1 | Joint fitting of VFA and Z-spectrum data

Three frameworks of data analysis were used to derive the quantitative maps of MT parameters ( $T_{2,f}$ ,  $T_{2,b}$ ,  $T_1$ , MPF, and the exchange rate R), combining VFA data with (i) SOFS Z-spectra and fitted by the qMT-noONRS model (SOFS-noONRS; “A”), (ii) SOFS Z-spectra and fitted by the qMT-ONRS model (SOFS-ONRS; “B”), and (iii) DOFS Z-spectra and fitted by the qMT-ONRS model (DOFS-ONRS; “C”). Hence, only the DOFS-ONRS framework is conceptually consistent, because it combines

a model that is adapted to the input data (no dipolar order). All reconstructions included transmit-field inhomogeneity correction of all pulse-related quantities in Eqs. (5) and (6), as provided by the estimated and resampled relative  $B_1^+$  map.

Comparison of the three frameworks was achieved by performing linear regression and Bland–Altman analyses on quantitative parameter values derived in WM and DGM regions.

Finally, the reproducibility of the DOFS-ONRS framework was assessed in a test–retest experiment. Bland–Altman and linear regression analyses of the estimated qMT parameters were performed between the two experiments. For each metric, the coefficients of variation ( $\text{CoV} = \text{SD}/\text{mean}$ ; between both sessions) averaged over all selected regions in WM and DGM regions were reported.

In Bland–Altman analyses, biases and limits of agreement (LOAs; defined as mean difference  $\pm 1.96$  SD of the mean difference) were reported. For each framework, the average values of parameters in ROIs and associated RMS error (RMSE) of the fits were calculated.

### 2.5.2 | Joint fitting of VFA and single-point MT data

The DOFS-ONRS framework was further extended following the single-point qMT approach<sup>7</sup>: VFA data and a single optimized and  $\text{MT}_0$ -normalized DOFS-MTw image were used jointly (JSP) for the simultaneous estimation of  $T_1$  and MPF while constraining other qMT parameters. In practice,  $R$ ,  $T_{2,b}$ , and the product  $R_1 \cdot T_{2,f}$  were fixed to the median values of the estimated parameter distributions from all voxels in the brain parenchyma over the 3 subjects, and as computed from the previous full Z-spectra DOFS-ONRS framework. Then, MPF and  $T_1$  maps were estimated for each possible experimental  $\Delta/B_{1,\text{RMS}}^{\text{SAT}}$  pair. The optimized DOFS-MTw image for JSP-qMT was selected as that yielding the minimum deviation ( $\delta_p$ ) in MPF and  $T_1$  values estimated in the whole-brain parenchyma relative to those obtained from the full spectra analysis.

$$\delta_p = \frac{1}{N} \sum_i^N \frac{|p_z^i - p_{\text{JSP}}^i|}{p_z^i} \quad (10)$$

where  $p_z^i$  and  $p_{\text{JSP}}^i$  are the estimated voxel values for  $p = \{T_1; \text{MPF}\}$  from full Z-spectrum and JSP-qMT, respectively. Linear regressions and Bland–Altman analyses were performed between both reconstructions over MPF and  $T_1$ .

## 3 | RESULTS

### 3.1 | Simulations

The theoretically expected biases on the estimation of qMT parameters caused by the dipolar order and ONRS effects are highlighted in the simulation results (Figure 2). Focusing on MPF and  $T_1$ , the relative variations between the reference and estimated values highlight systematic overestimation of  $T_1$  and underestimation of MPF for all values of  $T_{1D}$  under the combined effects of dipolar order and fits to the qMT-noONRS model (SOFS-noONRS), with relative biases more important in WM (Figure 2A,C) compared with GM (Figure 2B,D). Note that the bias remains fairly constant for  $T_1$ , whereas it diverges when  $T_{1D}$  increases for MPF, underlying the growing reduction of RF saturation effects of the macromolecular magnetization with  $T_{1D}$ . For  $T_{1D}$  values representative of in vivo conditions (i.e.,  $T_{1D} = 6.0$  ms/5.8 ms in WM/GM<sup>26</sup>), the relative variations were  $-11.6\%/ -9.0\%$  for MPF and  $5.8\%/3.2\%$  for  $T_1$ , corresponding to deviations (expressed in absolute units) of  $-1.7\%/ -0.8\%$  for MPF and  $63.3$  ms/51.4 ms for  $T_1$ . Correcting only for ONRS effects (SOFS-ONRS) removes the biases for  $T_{1D} < 100$   $\mu\text{s}$ , indicating that in this range of  $T_{1D}$  values and for the chosen saturation parameters, the dipolar order effects do not affect the qMT parameter estimations. Conversely, for  $T_{1D} > 100$   $\mu\text{s}$ , the absolute biases increase as  $T_{1D}$  increases for both MPF and  $T_1$ . For  $T_{1D}$  values representative of in vivo measurements, the relative variations induced by dipolar order effects were  $-3.7\%/ -3.9\%$  for MPF and only  $-0.5\%/ -0.3\%$  for  $T_1$ , corresponding to deviations (expressed in absolute units) of  $-0.6\%/ -0.3\%$  for MPF and  $-5.0$  ms/  $-4.7$  ms for  $T_1$ . Finally, under a complete decoupling condition of the macromolecular Zeeman and dipolar orders and accounting for ONRS effects (DOFS-ONRS), no deviation is expected for MPF and  $T_1$  ( $\text{RV} = 0\%$ ), regardless of  $T_{1D}$ . Details and descriptions of the simulation results for  $T_{2,f}$ ,  $T_{2,b}$ , and  $R$  are provided in Figure S5.

### 3.2 | Experiments

#### 3.2.1 | Comparison of frameworks

Figure 3A shows representative Z-spectra of SOFS-MT and DOFS-MT average signals in the anterior corona radiata. The dual-offset frequency pulses (black curves) yield a higher apparent saturation effect compared with single-offset frequency pulses (red curves). For both saturation strategies, signal attenuation increases with  $B_{1,\text{RMS}}^{\text{SAT}}$ . The difference between SOFS-MTw and DOFS-MTw normalized data is shown in Figure 3B and

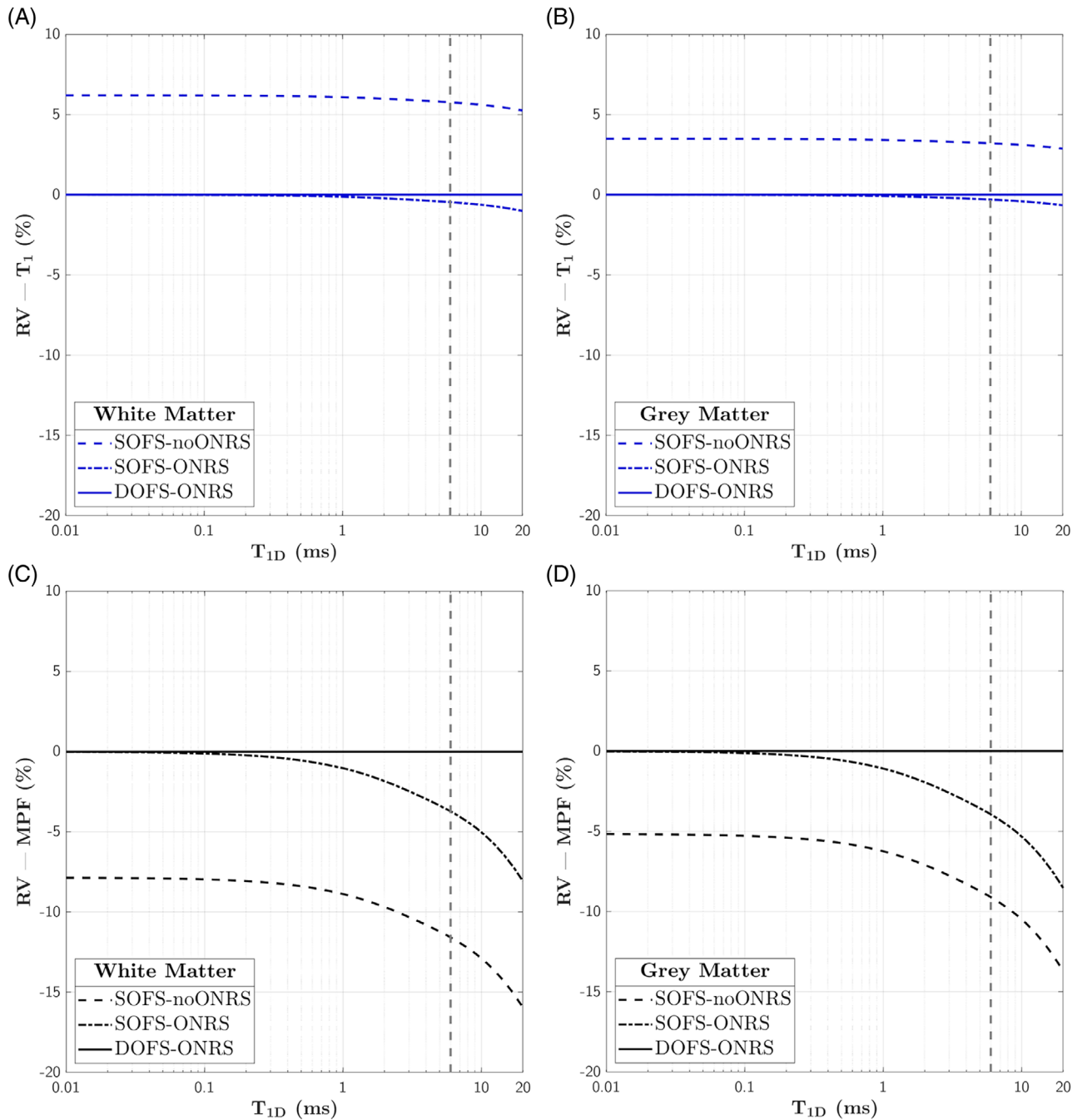


**FIGURE 2** Relative variations (RVs) between fixed-reference qMT parameters for  $T_1$  (A,B) and macromolecular proton fraction (MPF) (C,D) in white matter (WM; A,C) and gray matter (GM; B,D) and those estimated from synthetic data with dipolar order and fitted using the qMT-without on-resonance saturation (noONRS) model (SOFS-noONRS; point-dashed lines) and qMT-ONRS model (SOFS-ONRS; dashed lines), and from synthetic data without dipolar order and fitted with the qMT-ONRS model (DOFS-ONRS; solid lines). RVs are plotted as a function of  $T_{1D}$  for the following reference WM/GM qMT parameters:  $T_{2,f} = 20/30$  ms,  $T_{2,b} = 11/10$   $\mu$ s,  $T_1 = 1100/1600$  ms, MPF = 15/9%, and  $R = 20/20$  s<sup>-1</sup>. Dashed vertical gray lines refer to  $T_{1D}$  values estimated in WM ( $T_{1D} = 6.0$  ms; A,C) and GM ( $T_{1D} = 5.8$  ms; B,D), respectively.<sup>26</sup>

exhibits a bell-shaped curve peaking in the 1–4-kHz range, depending on  $B_{1,RMS}^{SAT}$ . The normalized signal difference corresponds to half of the ihMT ratio (ihMTR; with  $ihMTR = 2 \times [MTw^{SOFS} - MTw^{DOFS}]/MT_0$ ).<sup>46</sup> A representative normalized difference image for  $\Delta = 2$  kHz and  $B_{1,RMS}^{SAT} = 3.73$   $\mu$ T is provided in Figure S1.

Representative axial views of MPF and  $T_1$  maps are shown in Figure 4. A clear increase of MPF values can be appreciated in WM between maps derived from the frameworks SOFS-noONRS (Figure 4A), SOFS-ONRS (Figure 4B), and DOFS-ONRS (Figure 4C). Conversely, changes in  $T_1$  are less evident, although a slight decrease of



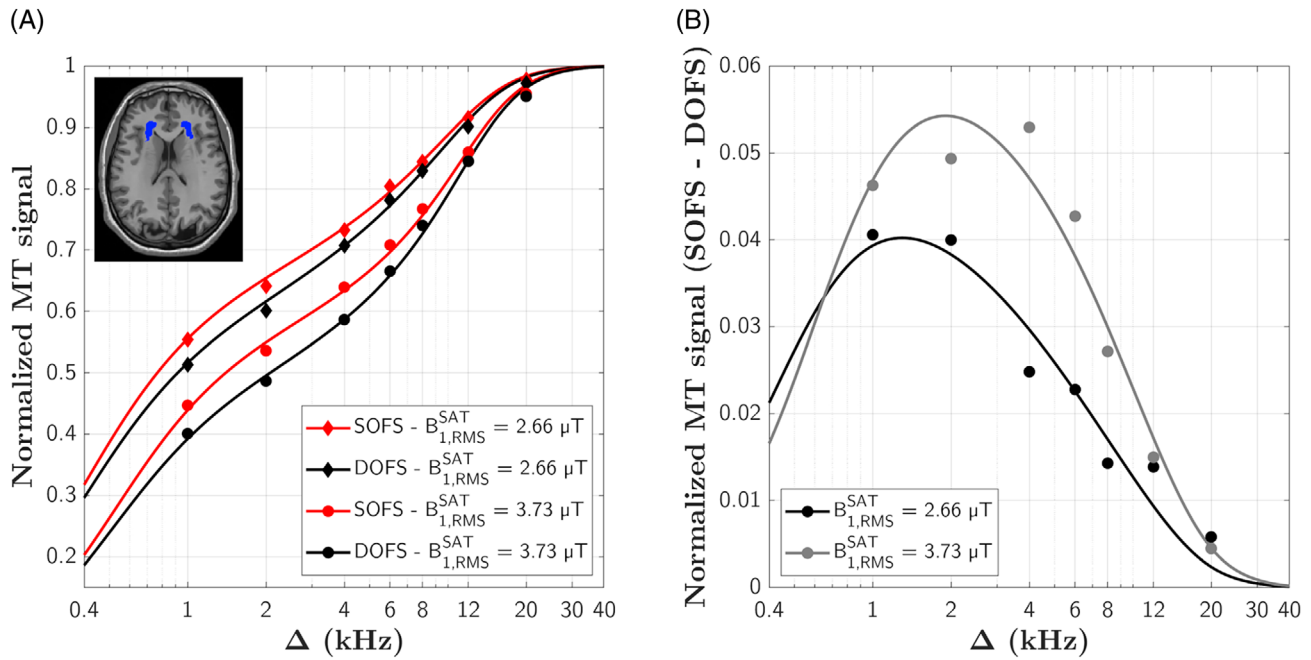


**FIGURE 3** (A) Representative Z-spectra of SOFS-MT (red) and DOFS-MT (black) signals from an averaged JHU region (anterior corona radiata; blue areas on the T<sub>1</sub>-weighted axial view). (B) Difference between SOFS-normalized and DOFS-normalized MT signals, corresponding to the inhomogeneous magnetization transfer ratio (ihMTR) signal divided by 2 ( $ihMTR = 2 \times [MTw^{SOFS} - MTw^{DOFS}] / MT_0$ )<sup>46</sup>.

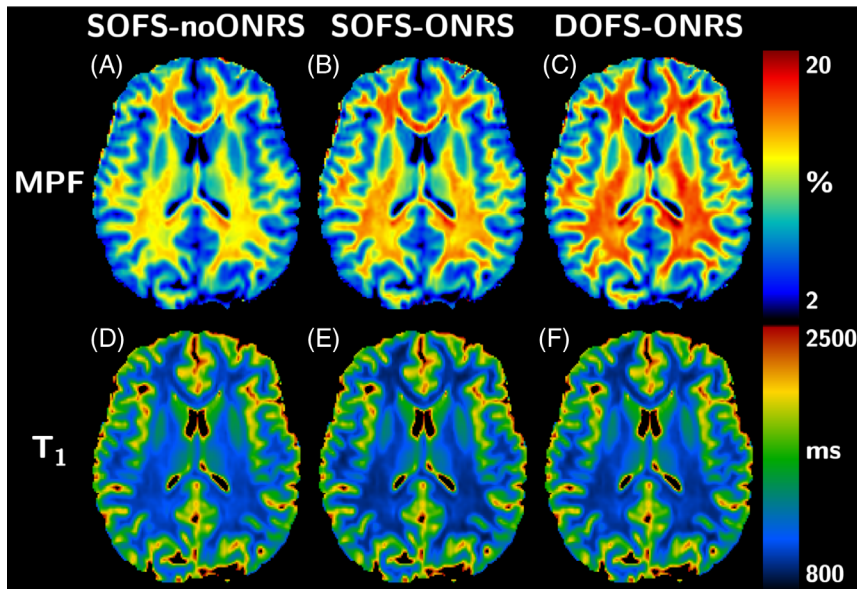


**FIGURE 4** Representative MPF and T<sub>1</sub> axial views derived from the SOFS-noONRS framework (SOFS-MTw data and qMT-noONRS model) (A,D), SOFS-ONRS framework (SOFS-MTw data and qMT-ONRS model) (B,E), and DOFS-ONRS framework (DOFS-MTw data and qMT-ONRS model) (C,F).

values in WM can be observed between the SOFS-noONRS framework (Figure 4D) and the two other frameworks (Figure 4E,F). Mean absolute values of qMT parameters averaged over the 3 subjects and the RMSE of the fits are reported in Table 1. Of interest, RMSE of the fits were significantly different (two-sampled t-test;  $p < 0.05$ ) only for average WM between frameworks DOFS-ONRS (mean RMSE = 8.06) and SOFS-noONRS (mean RMSE = 8.65) and SOFS-ONRS (mean RMSE = 8.63), but not in DGM (mean RMSE of 9.47, 9.43, and 9.35 for

frameworks SOFS-noONRS, SOFS-ONRS, and DOFS-ONRS, respectively).

Comparisons between frameworks are provided with the linear regressions and Bland–Altman plots for MPF (Figure 5) and T<sub>1</sub> (Figure 6). Other qMT parameters ( $R$ ,  $T_{2,b}$ , and  $T_{2,f}$ ) are reported and commented in Figures S6–S8.

The comparison between the SOFS-noONRS and DOFS-ONRS frameworks highlights the cumulative effect of dipolar order and ONRS contributions. Together, they

**TABLE 1** Summary of qMT-derived average values for MPF and  $T_1$  in WM and DGM and RMS error of the fits for qMT-noONRS applied to SOFS-MTw data (SOFS-noONRS framework), qMT-ONRS model applied to SOFS-MTw data (SOFS-ONRS framework), and qMT-ONRS model applied to DOFS-MTw data (DOFS-ONRS framework).

Structures	Framework SOFS-noONRS			Framework SOFS-ONRS			Framework DOFS-ONRS		
	MPF (%)	$T_1$ (ms)	RMSE ( $\times 10^3$ )	MPF (%)	$T_1$ (ms)	RMSE ( $\times 10^3$ )	MPF (%)	$T_1$ (ms)	RMSE ( $\times 10^3$ )
White matter									
Corpus callosum (genu)	14.4	1038.7	9.92	15.7	980.7	9.92	16.9	994.2	9.25
Corpus callosum (splenium)	14.0	1057.8	8.53	15.3	998.6	8.52	16.5	1012.4	8.12
Corpus callosum (body)	13.7	1055.0	8.29	15.0	994.9	8.29	16.3	1007.9	8.02
Cortico-spinal tracts	12.4	1290.7	11.11	13.6	1221.3	11.08	15.5	1239.8	8.44
Internal capsules	12.3	1088.9	8.45	13.4	1033.5	8.42	14.3	1044.2	7.98
Corona radiata	13.9	1034.1	7.04	15.3	970.9	7.00	16.7	983.4	6.72
Average (all WM regions)	<b>13.0</b>	<b>1116.9</b>	<b>8.65</b>	<b>14.2</b>	<b>1056.4</b>	<b>8.63</b>	<b>15.5</b>	<b>1069.8</b>	<b>8.06</b>
Deep gray matter									
Thalamus	9.5	1374.6	9.15	10.2	1321.8	9.14	11.4	1332.6	8.95
Caudate	7.0	1545.4	8.32	7.4	1504.5	8.30	8.1	1512.5	8.70
Putamen	7.8	1422.9	8.58	8.2	1379.7	8.55	9.2	1388.7	8.03
Pallidum	9.6	1252.5	8.45	10.3	1203.1	8.42	11.6	1214.8	7.93
Hippocampus	6.4	1770.8	10.19	6.8	1725.5	10.18	7.3	1733.4	10.48
Amygdala	6.5	1765.0	10.43	6.9	1719.7	10.39	7.6	1728.6	10.12
Average (all DGM regions)	<b>8.1</b>	<b>1496.9</b>	<b>9.47</b>	<b>8.7</b>	<b>1449.5</b>	<b>9.43</b>	<b>9.4</b>	<b>1458.3</b>	<b>9.35</b>

Abbreviation: RMSE, RMS error.

induced an important systematic underestimation of MPF ( $MPF^C = 1.22 \times MPF^A - 0.38\%$ ;  $R^2_{adj} = 0.98$ ; Figure 5B) and an overestimation of  $T_1$  ( $T_1^C = 1.02 \times T_1^A - 66.9$  ms;  $R^2_{adj} = 1.00$ ; Figure 6B). The corresponding biases in absolute value were, for MPF,  $-2.52\%$  ( $LOA = [-1.47; -3.56]\%$ ) in WM and  $-1.29\%$  ( $LOA = [-0.11; -2.48]\%$ ) in DGM (Figure 5A) and for  $T_1$ , 47.1 ms ( $LOA = [59.1/35.1]$  ms) in WM and 38.6 ms ( $LOA = [52.2/24.9]$  ms) in DGM (Figure 6A).

The comparison between the SOFS-ONRS and DOFS-ONRS frameworks highlights only the effect of dipolar order contributions, as ONRS effects are accounted for. A systematic, albeit more reduced, underestimation of MPF was also observed ( $MPF^C = 1.06 \times MPF^B + 0.31\%$ ;  $R^2_{adj} = 0.97$ ; Figure 5D). The corresponding biases were  $-1.30\%$  ( $LOA [-0.17; -2.44]\%$ ) in WM and  $-0.72\%$  ( $LOA [0.31; -1.75]\%$ ) in DGM (Figure 5C). Estimation of  $T_1$  was only marginally affected by the contribution of dipolar order ( $T_1^C = 0.99 \times T_1^B + 22.0$  ms;  $R^2_{adj} = 1.00$ , Figure 6D). Hence, the biases were small:  $-13.4$  ms ( $LOA [-7.6; -19.2]$  ms) in WM and  $-8.9$  ms ( $LOA [-2.1; -15.7]$  ms) in DGM (Figure 6C).

### 3.2.2 | Reproducibility

The reproducibility of the DOFS-ONRS framework is synthesized in the Bland–Altman and linear regression analyses performed between the test and retest experiments reported in Table 2. The best results were obtained for MPF (bias =  $-0.03\%$ ,  $LOA = [1.06; -1.13]\%$ ,  $CoV = 0.024 \pm 0.020$ ) followed by  $T_1$  (bias =  $-19.0$  ms,  $LOA = [65.5; -103.5]$  ms,  $CoV = 0.022 \pm 0.016$ ). Representative views of MPF and  $T_1$  maps are provided in Figure S2. Details on the reproducibility of  $T_{2,f}$ ,  $T_{2,b}$ , and R are provided in Table S2.

### 3.2.3 | Optimized joint single-point qMT

The minimum biases between MPF and  $T_1$  values estimated between the full Z-spectra and single  $\pm\Delta/B_{1,RMS}^{SAT}$  point analyses were obtained for  $\Delta = \pm 4$  kHz and  $B_{1,RMS}^{SAT} = 3.73$   $\mu T$  ( $\delta_{MPF} = 1.9\%$  and  $\delta_{T_1} = 0.16\%$ ; Figure S4), with R,  $R_1 \cdot T_{2,f}$ , and  $T_{2,b}$  fixed to  $21.1$   $s^{-1}$ , 0.0158, and 10.0  $\mu s$  (median values of brain parenchymal voxels; Figure S3). Note that very similar values ( $\delta_{MPF} = 2.1\%$

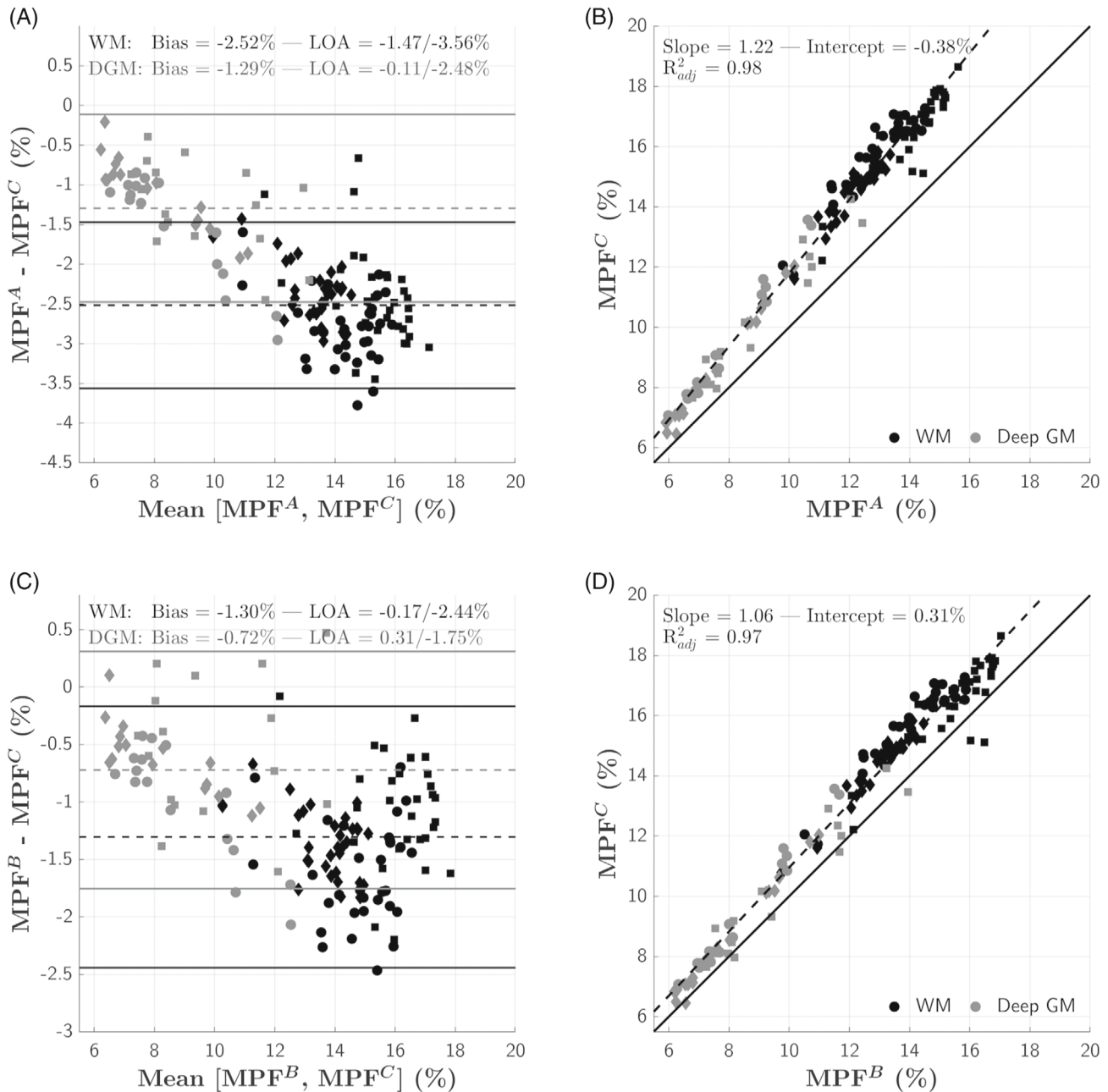


**FIGURE 5** Bland–Altman and linear regression plots between MPF values estimated from the three frameworks. (A,B) comparison between the SOFS-noONRS and DOFS-ONRS frameworks. (C,D) Comparison between the SOFS-ONRS and DOFS-ONRS frameworks. Mean bias and limits of agreements (LOAs) in Bland–Altman (A,C) plots are indicated in dashed and solid lines, respectively; values of WM and deep gray matter (DGM) are reported independently. Slopes and intercepts of the linear regression plots (B,D) were calculated from the joint distribution of WM and DGM values of the 3 subjects. Unity and regression lines are represented in full and dashed lines, respectively. Each subject is indicated by a different symbol (circle, diamond, and square). (A) *SOFS-noONRS*. (B) *SOFS-ONRS*. (C) *DOFS-ONRS*.

and  $\delta_{T_1} = 0.16\%$ ) were obtained at  $\Delta = \pm 4$  kHz and  $B_{1,RMS}^{SAT} = 2.66$   $\mu$ T. The corresponding MPF and  $T_1$  maps are shown in Figure 7, demonstrating a visually excellent consistency. Bland–Altman and linear regression analyses are shown in Figure 8. Excellent agreement was obtained for MPF (Figure 8A,B) with low biases of  $-0.15\%$  (LOA =  $[0.85/-1.15]\%$ ) in WM and  $0.10\%$

(LOA =  $[1.05/-0.85]\%$ ) in DGM, and a strong linear relationship (slope [intercept] =  $1.01$  [ $-0.09\%$ ];  $R^2_{adj} = 0.98$ ). Similarly,  $T_1$  was very consistent (Figure 8C,D), with biases of  $-3.5$  ms (LOA =  $[6.5/-13.5]$  ms) in WM and  $-1.6$  ms (LOA =  $[11.3/-14.5]$  ms) in DGM, and an excellent linear regression with slope [intercept] =  $1.00$  [ $8.1$  ms] ( $R^2_{adj} = 1.00$ ).

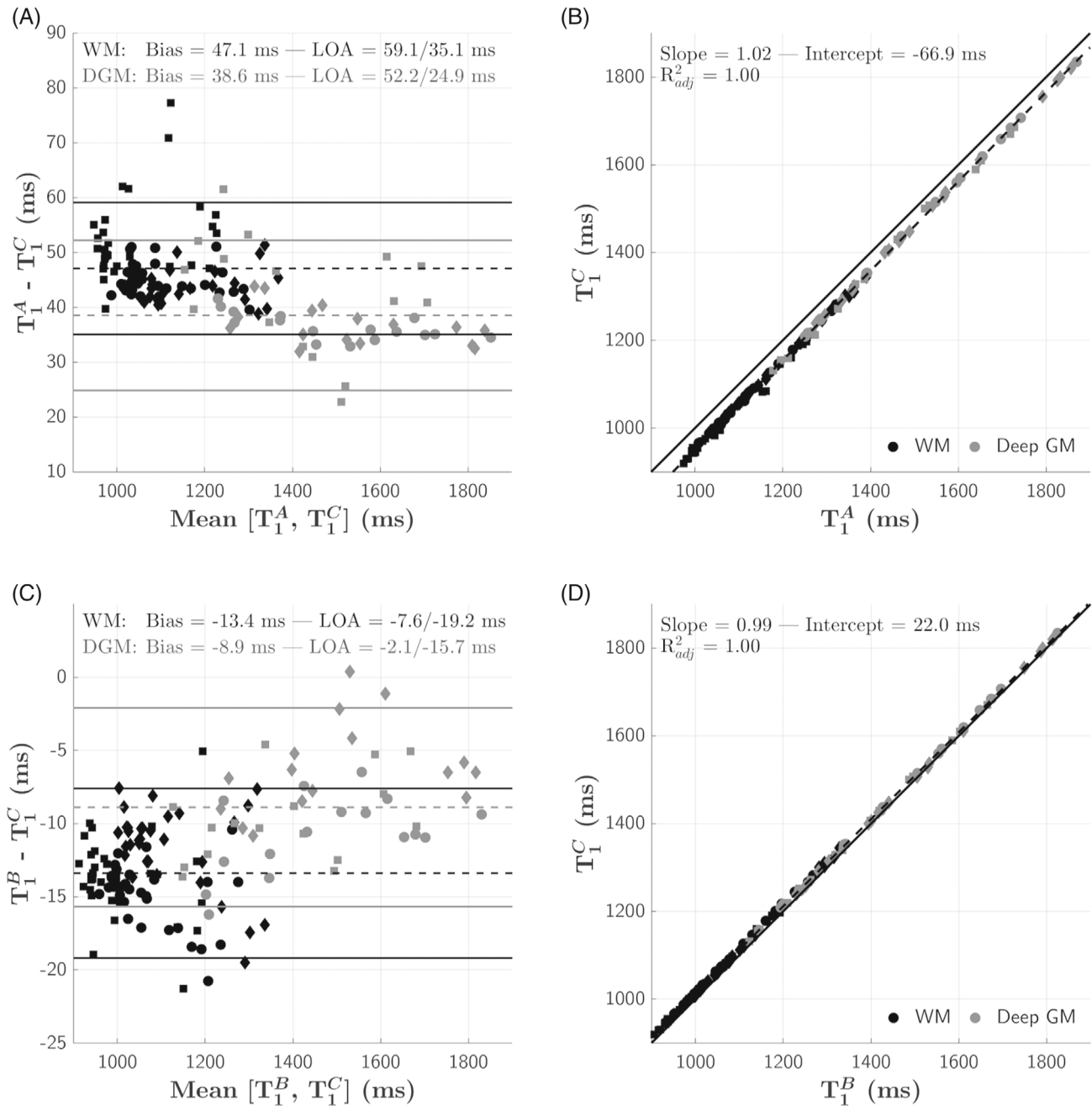


**FIGURE 6** Bland–Altman and linear regression plots between  $T_1$  values estimated from the three frameworks. (A,B) Comparison between the SOFS-noONRS and DOFS-ONRS frameworks. (C,D) Comparison between the SOFS-ONRS and DOFS-ONRS frameworks. Mean bias and LOAs in Bland–Altman (A,C) plots are indicated in dashed and solid lines, respectively; values of WM and DGM are reported independently. Slopes and intercepts of the linear regression plots (B,D) were calculated from the joint distribution of WM and DGM values of the 3 subjects. Unity and regression lines are represented in full and dashed lines, respectively. Each subject is indicated by a different symbol (circle, diamond, and square). (A) *SOFS-noONRS*. (B) *SOFS-ONRS*. (C) *DOFS-ONRS*.

## 4 | DISCUSSION

In this study, we demonstrated both theoretically and experimentally that dipolar order effects and MT effects induced by readout pulses in SPGR-based acquisitions can lead to biases in the MPF and  $T_1$  values estimated with the

standard two-pool qMT model. As a potential solution, we proposed a framework that uses DOFS pulses (canceling out dipolar order effects) combined with a two-pool qMT model that considers the ONRS of the readout pulses. This framework shows good performance in terms of reproducibility and is suitable for fast single-point qMT imaging.

**TABLE 2** Summary of qMT parameters of the reproducibility experiment estimated by the DOFS-ONRS framework and evaluated by Bland–Altman and linear regression analyses. The coefficient of variation between test and retest experiments are provided.

Parameter	Bland–Altman		Linear Regression			Coefficient of Variation
	Bias	LOAs	Slope	Intercept	$R_2^{\text{adj}}$	
MPF	−0.03%	1.05/−1.13%	0.98	0.31%	0.97	$0.024 \pm 0.020$
$T_1$	−19.0 ms	65.5/−103.5 ms	1.00	18.3 ms	0.97	$0.022 \pm 0.016$

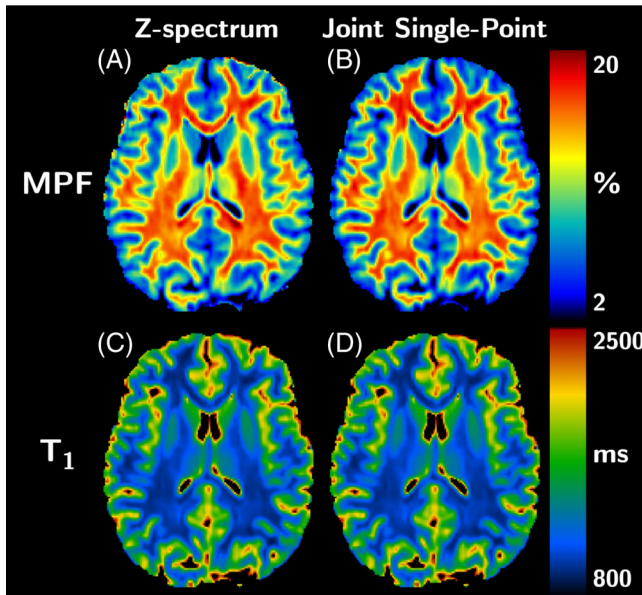


**FIGURE 7** Representative axial views of MPF (A,B) and  $T_1$  (C,D) maps from the DOFS data and qMT-ONRS model (DOFS-ONRS framework) using the full Z-spectrum data analysis (A,C) and the joint single-point MTw analysis (B,D), generated with  $\Delta = 4$  kHz and  $B_{1,\text{RMS}}^{\text{SAT}} = 3.73$   $\mu\text{T}$ .

#### 4.1 | Understanding and reducing biases in standard qMT-SPGR frameworks

The combined effects of dipolar order and ONRS lead to an underestimation of MPF and an overestimation of  $T_1$  when the standard qMT model and SOFS-based acquisitions are used. The amplitude of the theoretically expected biases estimated from simulated data were in line with experiments, with larger effects in WM in comparison to GM (Figures 2, 5 and 6, and Table 1). The overestimation of  $T_1$  was predominantly a consequence of ONRS effects, given the low difference in bias values between the SOFS-ONRS and DOFS-ONRS frameworks, which differ by the effect of dipolar order. Overall, this is consistent with already-established observations in ihMT studies, in which higher dipolar order effects are known to occur preferentially in WM compared with GM,<sup>22,23,32,46–48</sup> and further supported by the resulting mean RMSE significantly decreasing in WM from the SOFS-noONRS and

SOFS-ONRS frameworks to the DOFS-ONRS framework (Table 1). Overall, accounting for ONRS effects almost cancels  $T_1$ -related biases, whereas dipolar order effects need to be removed to minimize MPF-related biases, hence making the binary spin-bath model appropriate to process the data.

In most qMT-SPGR frameworks, MT effects occurring in VFA experiments are not modeled (i.e., ONRS are not considered) and dipolar order effects are neglected, despite the use of SOFS pulses.<sup>5,7,49–55</sup> As a result, the estimated qMT parameter values remain dependent on the experimental conditions ( $\Delta$ ,  $B_{1,\text{RMS}}^{\text{SAT}}$ , readout flip angles, and sequence delays); hence, different protocols prevent consistent reporting and cross-platform reproducibility. More specifically, variations related to  $\Delta$  and  $B_{1,\text{RMS}}^{\text{SAT}}$  parameters—and intrinsically to the saturation pulse shape—strongly influence the resulting  $T_{1D}$ -weighting effects when relying on SOFS data,<sup>29</sup> and hence the apparent MT weighting.

The proposed DOFS-ONRS framework was designed to remove dipolar order effects and therefore to make the two-pool model suitable. It has demonstrated a good intrasession reproducibility, thereby representing a promising solution for cross-scanner investigations. Studies on animals with preclinical scanners are likely to be affected by similar biases, hence calling for similar sequence implementations and analyses. This is even more important for translational purposes, as the MPF or its equivalents (e.g., pool size ratio) can be used to synthesize biomarkers such as the g-ratio.<sup>56–58</sup>

#### 4.2 | Fast MPF and $T_1$ mapping

We demonstrated the feasibility of fast joint MPF and  $T_1$  mapping using the derived JSP-qMT method, and within the optimized and accurate DOFS-ONRS framework (Figures 7 and 8) with a good agreement between full Z-spectrum and JSP-qMT outputs, resulting in a total acquisition time of 6 min 25 s for a 2-mm isotropic resolution. The method, as proposed, requires a minimum of five images: a pair of MTw and  $MT_0$  SPGR images, unsaturated proton density-weighted and  $T_1$ -weighted SPGR-images, and a  $B_1^+$  map. Of interest, the constrained values for R

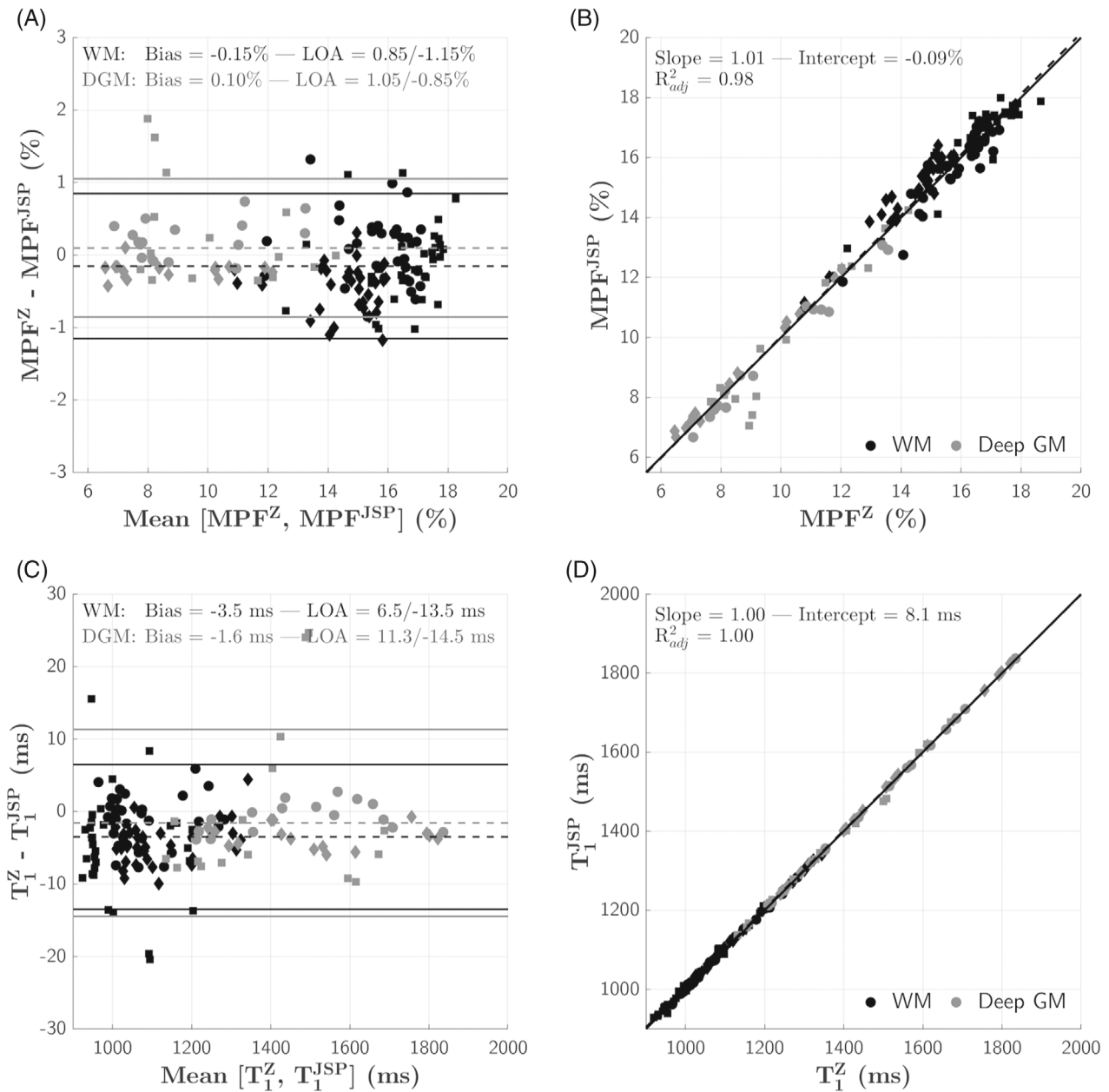


**FIGURE 8** Bland–Altman and linear regression plots of MPF (A,B) and  $T_1$  (C,D) estimated from full DOFS Z-spectra analysis (Z) and joint single-point (JSP) DOFS data analysis. Bias and LOAs are indicated in dashed and solid lines, respectively, in Bland–Altman plots. Regression and unity lines are depicted as dashed and solid lines, respectively, in regression plots. Biases and LOAs in WM and DGM are reported independently, whereas the reported slopes and intercepts of the linear regression were calculated from the joint distributions. Each subject is depicted by a different symbol (circle, diamond, and square).

and  $T_{2,b}$  are rather close to that estimated by Yarnykh<sup>7</sup> at 3 T ( $R = 21.1 \text{ s}^{-1}$  vs.  $19.0 \text{ s}^{-1}$  and  $T_{2,b} = 10.0 \mu\text{s}$  vs.  $9.7 \mu\text{s}$ ), while the product  $R_1 \cdot T_{2,f}$  is reduced ( $R_1 \cdot T_{2,f} = 0.016$  vs.  $0.022$ ). Applicability of this methodology to pathologies (e.g., multiple sclerosis) and animal models (e.g., cuprizone<sup>59</sup> and experimental autoimmune encephalomyelitis<sup>60</sup>) nonetheless requires a dedicated validation on respective subjects, although previous works revealed very close values of the constrained qMT parameters between healthy and nonhealthy groups.<sup>7,55</sup>

### 4.3 | Future biophysical and mathematical modeling

In this work, we expanded on the classical two-pool model methodology<sup>3,61</sup> that has raised interest over the last two decades because of its simplicity, practicability, and reproducibility.<sup>52</sup> More advanced models may help provide better understanding of the MT signal behavior in brain tissues, the most common application of qMT.<sup>53</sup> This is highlighted here by the discrepancies in the exchange rate

when fitting SOFS and DOFS data (Figure S6), which complements the difference in values between classical qMT frameworks ( $R \approx 20 \text{ s}^{-1}$ )<sup>7,50,54,55</sup> and that found in quantitative ihMT frameworks ( $R$  spanning from 20 to  $70 \text{ s}^{-1}$ , depending on the compartmental model).<sup>32</sup> As a perspective, more detailed models could lead to a better description of myelinated brain tissues. For instance, the four-pool model—recently documented quite comprehensively by Manning et al.<sup>62</sup>—considers two exchanging myelin and nonmyelin water pools, respectively exchanging with the myelin and nonmyelin macromolecular matrices. In addition, evidence was found that multiple dipolar order reservoirs exist in myelinated tissues<sup>25</sup> and in synthesized lipid samples representative of myelin,<sup>63</sup> and their intrinsic association to macromolecular Zeeman reservoirs (with respective and distinct MT parameters) has yet to be investigated. Of note, the proposed DOFS-MTW acquisitions effectively remove the need to consider the dipolar order magnetization reservoirs, and the qMT-ONRS model remains valid as long as the respective exchange rate and macromolecular  $T_{2,b}$  parameters are considered equal, contrary to the fitting of SOFS-based acquisitions for which the impact of dipolar order reservoir on the saturation attenuation is less predictable. Note also that equality between the two pools' relaxation times ( $T_{1,f} = T_{1,b}$ ) was assumed. Although this is a common hypothesis in standard qMT analyses,<sup>7,10,36,64,65</sup> some studies have reported shorter values for the estimated  $T_{1,b}$  in healthy human brain WM.<sup>66,67</sup> Upgrading the current models to allow for the discrimination of multiple free and bound Zeeman reservoirs would necessitate accumulation of a high number of images with varying sequence parameters, and for which classical Z-spectra acquisitions (i.e., varying  $\Delta$  and  $B_{1,\text{RMS}}^{\text{SAT}}$ ) may not be sufficient to yield an adequate sensitivity to the parameters. Further investigation is therefore warranted.

Perfect transverse-magnetization spoiling (i.e., complete extinction of  $M_{xy}^f$  just before the readout pulse in this case) is a pervasive assumption made in VFA and qMT mathematical models—here numerically achieved with the “ $\phi$ ” matrix in Eq. (8). However, slight deviations of the experimental signal from Eq. (8) may occur and depend primarily on the apparent tissue parameters (e.g.,  $T_1$ ,  $T_2$ , diffusion coefficients, and MT parameters) and local  $B_1^+$ .<sup>12,68,69</sup> Gradient spoiling–induced transverse magnetization attenuation through diffusion effects, in addition to the RF spoiling, helps in mitigating such effects but remains mildly efficient with standard clinical systems, and depends on hardware capacities and resolutions.<sup>69–71</sup> This calls for deepened modeling of the signal behavior using the configuration states formalism, to account for these effects,<sup>12,72</sup> at the cost of a substantial computational burden with regard to the voxelwise inverse problem

solving. Further investigation is therefore warranted on the contributions of imperfect spoiling effects about the estimated qMT parameters.

The longitudinal magnetization attenuation of the free pool during the application of an off-resonance RF pulse is classically calculated using a Lorentzian lineshape for the calculation of the absorption rate ( $W_f^{\text{SAT}}$ ), assuming a constant RF saturation pulse applied at an exact frequency  $\Delta$ . Recent work showed the effect of the off-resonance pulse shape and duration, which yielded complex effects straightforwardly related to an on-resonance spectral leakage, affecting the free pool magnetization<sup>34</sup> (also referred to as direct saturation effects). These results emphasize the modeling limitation of  $W_f^{\text{SAT}}$  when using finite RF pulse whose spectral response depends on the pulse shape, duration and power, and remain important for the estimation of  $T_{2,f}$ , as the parameter's sensitivity is localized at low offset frequencies.<sup>7,55</sup>

In this work, we used a super-Lorentzian absorption lineshape, including a residual broadening<sup>35</sup> term (mostly affecting the on-resonance part of the line), for the calculation of the macromolecular absorption rates ( $W_b^{\text{SAT}}$  and  $W_b^{\text{RO}}$ ), as it represents a more legitimate alternative to the extrapolation method for on-resonance saturation.<sup>12,36</sup> However, bandwidth effects of the finite readout pulse are not considered in the calculation of  $W_b^{\text{RO}}$ , and its subsequent effect on the parameters' estimation may still depend on the readout pulse power, shape and duration, as the absorption lineshape varies rapidly around the resonance. As such, we chose a rather spectrally concentrated and spatially nonselective Hann-shaped pulse for readout with a reasonable duration ( $\tau_{\text{RO}} = 1 \text{ ms}$ ) instead of seemingly often used short rectangular pulses that may exhibit a large spectral response with nonnegligible sinc ripples.

In the proposed DOFS-ONRS framework, VFA data provided the necessary sensitivity to longitudinal relaxation. Although SPGR sequences are attractive for their simplicity, acquiring high-resolution images requires an important acquisition time increase, for which advanced acceleration methods such as compressed sensing<sup>73</sup> should be beneficial. Alternatively, as an efficient high-resolution solution, the widely used MP2RAGE sequence<sup>74</sup>—which also has been shown to be sensitive to MT effects<sup>75</sup>—may substitute the VFA-SPGR protocol to provide the desired  $T_1$  sensitization, and by adapting the DOFS-ONRS framework to encompass an advanced MP2RAGE signal model.

## 5 | CONCLUSIONS

SOFS-prepared SPGR acquisitions are inconsistent with the classical binary spin-bath model, which does not

account for dipolar order and associated relaxation ( $T_{1D}$ ) effects. In this study, we have documented how this model inconsistency biases the estimated qMT parameters. In addition, we also showed that MT effects arising from the on-resonance saturation and exchanges during a VFA experiment can lead to biases on apparent  $T_1$  and MPF estimations. The present work demonstrated the importance of sequence design and signal modeling in quantitative MT imaging. For the sake of reproducibility and accuracy, we therefore encourage investigators to systematically consider all MT effects in models. The use of DOFS pulses in MT-prepared SPGR experiments eliminates dipolar order-related errors in qMT and is therefore recommended for future studies.

### ACKNOWLEDGMENTS

This work was supported by the French National Research Agency, ANR (ANR-17-CE18-0030, ANR-22-CE18-0041, and ANR-22-CE17-0060), and ARSEP 2020. This work was performed by a laboratory member of France Life Imaging network (grant ANR-11-INBS-0006).

### CONFLICT OF INTEREST


Thomas Troalen is an employee at Siemens Healthcare. David C. Alsop receives institutional postmarket royalties for MRI inventions unrelated to this work from GE Healthcare, Siemens Healthineers, Philips Healthcare, Hitachi Medical, UIH America, and Animage LLC.

### DATA AVAILABILITY STATEMENT

The prototype MT-prepared SPGR sequence “vibeMT” used in experiments is available on the constructor Siemens C2P platform. A *MATLAB* (The MathWorks, Natick, Massachusetts, USA) implementation of the simulations is made available at <https://archive.softwareheritage.org/browse/directory/e6ecf00ebd02ffaf5522053fae189c58e11fa339/>). A processing code for the joint estimation of MPF and  $T_1$  based on the DOFS-ONRS framework is available at <https://github.com/lsoustelle/qMT>. The experimental data are not publicly available due to ethics restrictions.

### ORCID

Lucas Soustelle  <https://orcid.org/0000-0002-4688-3262>

Thomas Troalen  <https://orcid.org/0000-0002-5764-4689>

Andreea Hertanu  <https://orcid.org/0000-0003-2464-7872>


Jean-Philippe Ranjeva  <https://orcid.org/0000-0001-8073-102X>

Maxime Guye  <https://orcid.org/0000-0002-4435-2257>

Gopal Varma  <https://orcid.org/0000-0002-7060-1982>

David C. Alsop  <https://orcid.org/0000-0002-8206-1995>

Guillaume Duhamel  <https://orcid.org/0000-0001-5704-8513>

Olivier M. Girard  <https://orcid.org/0000-0002-5296-638X>

### TWITTER

Lucas Soustelle  @LucasSoustelle

### REFERENCES

- Edzes HT, Samulski ET. Cross relaxation and spin diffusion in the proton NMR of hydrated collagen. *Nature*. 1977;265:521-523. doi:10.1038/265521a0
- Grad J, Bryant RG. Nuclear magnetic cross-relaxation spectroscopy. *J Magn Reson*. 1990;90:1-8. doi:10.1016/0022-2364(90)90361-C
- Henkelman RM, Huang X, Xiang Q-S, Stanisz GJ, Swanson SD, Bronskill MJ. Quantitative interpretation of magnetization transfer. *Magn Reson Med*. 1993;29:759-766. doi:10.1002/mrm.1910290607
- Sled JG, Pike GB. Quantitative imaging of magnetization transfer exchange and relaxation properties in vivo using MRI. *Magn Reson Med*. 2001;46:923-931. doi:10.1002/mrm.1278
- Yarnykh VL, Bowen JD, Samsonov A, et al. Fast whole-brain three-dimensional macromolecular proton fraction mapping in multiple sclerosis. *Radiology*. 2015;274:210-220. doi:10.1148/radiol.14140528
- Corrigan NM, Yarnykh VL, Hippe DS, et al. Myelin development in cerebral gray and white matter during adolescence and late childhood. *Neuroimage*. 2021;227:117678. doi:10.1016/j.neuroimage.2020.117678
- Yarnykh VL. Fast macromolecular proton fraction mapping from a single off-resonance magnetization transfer measurement. *Magn Reson Med*. 2012;68:166-178. doi:10.1002/mrm.23224
- Yarnykh VL. Time-efficient, high-resolution, whole brain three-dimensional macromolecular proton fraction mapping. *Magn Reson Med*. 2016;75:2100-2106. doi:10.1002/mrm.25811
- Yarnykh VL. Data-driven retrospective correction of B1 field inhomogeneity in fast macromolecular proton fraction and R1 mapping. *IEEE Trans Med Imaging*. 2021;40:3473-3484. doi:10.1109/TMI.2021.3088258
- Mossahebi P, Yarnykh VL, Samsonov A. Analysis and correction of biases in cross-relaxation MRI due to biexponential longitudinal relaxation. *Magn Reson Med*. 2014;71:830-838. doi:10.1002/mrm.24677
- van Gelderen P, Jiang X, Duyn JH. Effects of magnetization transfer on T1 contrast in human brain white matter. *Neuroimage*. 2016;128:85-95. doi:10.1016/j.neuroimage.2015.12.032
- Malik SJ, Teixeira RPAG, Hajnal JV. Extended phase graph formalism for systems with magnetization transfer and exchange. *Magn Reson Med*. 2018;80:767-779. doi:10.1002/mrm.27040
- Teixeira RPAG, Malik SJ, Hajnal JV. Fast quantitative MRI using controlled saturation magnetization transfer. *Magn Reson Med*. 2019;81:907-920. doi:10.1002/mrm.27442
- Soustelle L, Troalen T, Hertanu A, et al. On the variability of single-point MPF mapping in the human brain using different variable flip angle T1 mapping protocols.



- Proceedings 29th Annual Meeting of ISMRM, Virtual meeting; ISMRM; 2021:498.*
15. Yeung HN, Adler RS, Swanson SD. Transient decay of longitudinal magnetization in heterogeneous spin systems under selective saturation. IV. Reformulation of the spin-Bath-model equations by the Redfield-Provotorov theory. *J Magn Reson Ser A.* 1994;106:37-45. doi:10.1006/jmra.1994.1004
  16. Provotorov BN. Magnetic resonance saturation in crystals. *Sov Phys JETP-USSR.* 1962;14:1126-1131.
  17. Morrison C, Stanisz G, Henkelman RM. Modeling magnetization transfer for biological-like systems using a semi-solid pool with a super-Lorentzian lineshape and dipolar reservoir. *J Magn Reson Ser B.* 1995;108:103-113. doi:10.1006/jmrb.1995.1111
  18. Sled JG, Pike GB. Quantitative interpretation of magnetization transfer in spoiled gradient echo MRI sequences. *J Magn Reson.* 2000;145:24-36. doi:10.1006/jmre.2000.2059
  19. Prevost VH, Yung A, Morris SR, et al. Temperature dependence and histological correlation of inhomogeneous magnetization transfer and myelin water imaging in ex vivo brain. *Neuroimage.* 2021;236:118046. doi:10.1016/j.neuroimage.2021.118046
  20. Fritz F, Helms G, Vaculčíaková L, Weiskopf N, Mohammadi S. Effects of temperature in the estimation of inhomogeneous magnetic transfer (ihMT) in post-mortem human brain. *Proceedings of the 31st Annual Meeting of ISMRM; ISMRM, London, UK, 2022:2712.*
  21. Swanson SD, Malyarenko DI, Fabiilli ML, Welsh RC, Nielsen J-F, Srinivasan A. Molecular, dynamic, and structural origin of inhomogeneous magnetization transfer in lipid membranes. *Magn Reson Med.* 2017;77:1318-1328. doi:10.1002/mrm.26210
  22. Hertanu A, Soustelle L, Le Troter A, et al. T1D-weighted ihMT imaging. Part I. Isolation of long- and short-T1D components by T1D-filtering. *Magn Reson Med.* 2022;87:2313-2328. doi:10.1002/mrm.29139
  23. Hertanu A, Soustelle L, Buron J, et al. T1D-weighted ihMT imaging. Part II. Investigating the long- and short-T1D components correlation with myelin content. Comparison with R1 and the macromolecular proton fraction. *Magn Reson Med.* 2022;87:2329-2346. doi:10.1002/mrm.29140
  24. Hertanu A, Soustelle L, Buron J, et al. Inhomogeneous magnetization transfer (ihMT) imaging in the acute cuprizone mouse model of demyelination/remyelination. *Neuroimage.* 2023;265:119785. doi:10.1016/j.neuroimage.2022.119785
  25. Carvalho VND, Hertanu A, Grélard A, et al. MRI assessment of multiple dipolar relaxation time (T1D) components in biological tissues interpreted with a generalized inhomogeneous magnetization transfer (ihMT) model. *J Magn Reson.* 2020;311:106668. doi:10.1016/j.jmr.2019.106668
  26. Varma G, Girard OM, Prevost VH, Grant AK, Duhamel G, Alsop DC. In vivo measurement of a new source of contrast, the dipolar relaxation time, T1D, using a modified inhomogeneous magnetization transfer (ihMT) sequence. *Magn Reson Med.* 2017;78:1362-1372. doi:10.1002/mrm.26523
  27. West DJ, Cruz G, Teixeira RPAG, et al. An MR fingerprinting approach for quantitative inhomogeneous magnetization transfer imaging. *Magn Reson Med.* 2022;87:220-235. doi:10.1002/mrm.28984
  28. Alsop DC, Ercan E, Girard OM, et al. Inhomogeneous magnetization transfer imaging: concepts and directions for further development. *NMR Biomed.* 2022 Aug 2:e4808. doi:10.1002/nbm.4808
  29. Manning AP, Chang KL, MacKay AL, Michal CA. The physical mechanism of "inhomogeneous" magnetization transfer MRI. *J Magn Reson.* 2017;274:125-136. doi:10.1016/j.jmr.2016.11.013
  30. Mchinda S, Varma G, Prevost VH, et al. Whole brain inhomogeneous magnetization transfer (ihMT) imaging: sensitivity enhancement within a steady-state gradient echo sequence. *Magn Reson Med.* 2018;79:2607-2619. doi:10.1002/mrm.26907
  31. Prevost VH, Girard OM, Mchinda S, Varma G, Alsop DC, Duhamel G. Optimization of inhomogeneous magnetization transfer (ihMT) MRI contrast for preclinical studies using dipolar relaxation time (T1D) filtering. *NMR Biomed.* 2017;30:e3706. doi:10.1002/nbm.3706
  32. Varma G, Girard OM, Prevost VH, Grant AK, Duhamel G, Alsop DC. Interpretation of magnetization transfer from inhomogeneously broadened lines (ihMT) in tissues as a dipolar order effect within motion restricted molecules. *J Magn Reson.* 2015;260:67-76. doi:10.1016/j.jmr.2015.08.024
  33. Lee J-S, Khitrin AK, Regatte RR, Jerschow A. Uniform saturation of a strongly coupled spin system by two-frequency irradiation. *J Chem Phys.* 2011;134:234504. doi:10.1063/1.3600758
  34. Soustelle L, Troalen T, Hertanu A, et al. A strategy to reduce the sensitivity of inhomogeneous magnetization transfer (ihMT) imaging to radiofrequency transmit field variations at 3 T. *Magn Reson Med.* 2022;87:1346-1359. doi:10.1002/mrm.29055
  35. Pampel A, Müller DK, Anwender A, Marschner H, Möller HE. Orientation dependence of magnetization transfer parameters in human white matter. *Neuroimage.* 2015;114:136-146. doi:10.1016/j.neuroimage.2015.03.068
  36. Gloor M, Scheffler K, Bieri O. Quantitative magnetization transfer imaging using balanced SSFP. *Magn Reson Med.* 2008;60:691-700. doi:10.1002/mrm.21705
  37. Malik SJ, Teixeira RPAG, West DJ, Wood TC, Hajnal JV. Steady-state imaging with inhomogeneous magnetization transfer contrast using multiband radiofrequency pulses. *Magn Reson Med.* 2020;83:935-949. doi:10.1002/mrm.27984
  38. Soustelle L, Troalen T, Hertanu A, et al. Quantitative magnetization transfer parametric mapping unbiased by on-resonance saturation and dipolar order contributions. *Proceedings of the 31st Annual Meeting of ISMRM; ISMRM, London, UK; 2022:2709.*
  39. Veraart J, Novikov DS, Christiaens D, Ades-aron B, Sijbers J, Fieremans E. Denoising of diffusion MRI using random matrix theory. *Neuroimage.* 2016;142:394-406. doi:10.1016/j.neuroimage.2016.08.016
  40. Grussu F, Battiston M, Veraart J, et al. Multi-parametric quantitative in vivo spinal cord MRI with unified signal readout and image denoising. *Neuroimage.* 2020;217:116884. doi:10.1016/j.neuroimage.2020.116884
  41. Tournier J-D, Smith R, Raffelt D, et al. MRtrix3: a fast, flexible and open software framework for medical image processing and visualisation. *Neuroimage.* 2019;202:116137. doi:10.1016/j.neuroimage.2019.116137
  42. Wakana S, Caprihan A, Panzenboeck MM, et al. Reproducibility of quantitative tractography methods applied to cerebral white matter. *Neuroimage.* 2007;36:630-644. doi:10.1016/j.neuroimage.2007.02.049
  43. Avants BB, Tustison NJ, Song G, Cook PA, Klein A, Gee JC. A reproducible evaluation of ANTs similarity metric performance in brain image registration. *Neuroimage.* 2011;54:2033-2044. doi:10.1016/j.neuroimage.2010.09.025

44. Avants BB, Tustison N, Song G. Advanced normalization tools (ANTS). *Insight J.* 2009;2:1-35.
45. Dale AM, Fischl B, Sereno MI. Cortical surface-based analysis. *Neuroimage.* 1999;9:179-194. doi:10.1006/nimg.1998.0395
46. Varma G, Duhamel G, de Bazelaire C, Alsop DC. Magnetization transfer from inhomogeneously broadened lines: a potential marker for myelin. *Magn Reson Med.* 2015;73:614-622. doi:10.1002/mrm.25174
47. Girard OM, Callot V, Prevost VH, et al. Magnetization transfer from inhomogeneously broadened lines (ihMT): improved imaging strategy for spinal cord applications. *Magn Reson Med.* 2017;77:581-591. doi:10.1002/mrm.26134
48. Duhamel G, Prevost VH, Cayre M, et al. Validating the sensitivity of inhomogeneous magnetization transfer (ihMT) MRI to myelin with fluorescence microscopy. *Neuroimage.* 2019;199:289-303. doi:10.1016/j.neuroimage.2019.05.061
49. Underhill HR, Rostomily RC, Mikheev AM, Yuan C, Yarnykh VL. Fast bound pool fraction imaging of the in vivo rat brain: association with myelin content and validation in the C6 glioma model. *Neuroimage.* 2011;54:2052-2065. doi:10.1016/j.neuroimage.2010.10.065
50. Underhill HR, Yuan C, Yarnykh VL. Direct quantitative comparison between cross-relaxation imaging and diffusion tensor imaging of the human brain at 3.0 T. *Neuroimage.* 2009;47:1568-1578. doi:10.1016/j.neuroimage.2009.05.075
51. Yarnykh VL, Yuan C. Cross-relaxation imaging reveals detailed anatomy of white matter fiber tracts in the human brain. *Neuroimage.* 2004;23:409-424. doi:10.1016/j.neuroimage.2004.04.029
52. Yarnykh VL, Kisel AA, Khodanovich MY. Scan-rescan repeatability and impact of B(0) and B(1) field nonuniformity corrections in single-point whole-brain macromolecular proton fraction mapping. *J Magn Reson Imaging.* 2020;51:1789-1798. doi:10.1002/jmri.26998
53. Kisel AA, Naumova AV, Yarnykh VL. Macromolecular proton fraction as a myelin biomarker: principles, validation, and applications. *Front Neurosci.* 2022;16:1-10. doi:10.3389/fnins.2022.819912
54. Naumova AV, Akulov AE, Khodanovich MY, Yarnykh VL. High-resolution three-dimensional macromolecular proton fraction mapping for quantitative neuroanatomical imaging of the rodent brain in ultra-high magnetic fields. *Neuroimage.* 2017;147:985-993. doi:10.1016/j.neuroimage.2016.09.036
55. Soustelle L, Antal MC, Lamy J, Harsan L, Loureiro de Sousa P. Determination of optimal parameters for 3D single-point macromolecular proton fraction mapping at 7T in healthy and demyelinated mouse brain. *Magn Reson Med.* 2021;85:369-379. doi:10.1002/mrm.28397
56. Mohammadi S, Callaghan MF. Towards in vivo g-ratio mapping using MRI: unifying myelin and diffusion imaging. *J Neurosci Methods.* 2020;348:108990. doi:10.1016/j.jneumeth.2020.108990
57. Campbell JSW, Leppert IR, Narayanan S, et al. Promise and pitfalls of g-ratio estimation with MRI. *Neuroimage.* 2017;182:1-17. doi:10.1016/j.neuroimage.2017.08.038
58. Stikov N, Campbell JSW, Stroh T, et al. In vivo histology of the myelin g-ratio with magnetic resonance imaging. *Neuroimage.* 2015;118:397-405. doi:10.1016/j.neuroimage.2015.05.023
59. Praet J, Guglielmetti C, Berneman Z, Van der Linden A, Ponsaerts P. Cellular and molecular neuropathology of the cuprizone mouse model: clinical relevance for multiple sclerosis. *Neurosci Biobehav Rev.* 2014;47:485-505. doi:10.1016/j.neubiorev.2014.10.004
60. Constantinescu CS, Farooqi N, O'Brien K, Gran B. Experimental autoimmune encephalomyelitis (EAE) as a model for multiple sclerosis (MS). *Br J Pharmacol.* 2011;164:1079-1106. doi:10.1111/j.1476-5381.2011.01302.x
61. Morrison C, Mark HR. A model for magnetization transfer in tissues. *Magn Reson Med.* 1995;33:475-482. doi:10.1002/mrm.1910330404
62. Manning AP, MacKay AL, Michal CA. Understanding aqueous and non-aqueous proton T1 relaxation in brain. *J Magn Reson.* 2021;323:106909. doi:10.1016/j.jmr.2020.106909
63. Hertanu A, Soustelle L, de Rochefort L, et al. Quantitative T1D assessment in lipid membranes: Jeener-Broekaert NMR vs. ihMT MRI. *Proceedings of the 31st Annual Meeting of ISMRM; ISMRM, London, UK; 2022:1422.*
64. Cronin MJ, Xu J, Bagnato F, Gochberg DF, Gore JC, Dortch RD. Rapid whole-brain quantitative magnetization transfer imaging using 3D selective inversion recovery sequences. *Magn Reson Imaging.* 2020;68:66-74. doi:10.1016/j.mri.2020.01.014
65. Dortch RD, Li K, Gochberg DF, et al. Quantitative magnetization transfer imaging in human brain at 3 T via selective inversion recovery. *Magn Reson Med.* 2011;66:1346-1352. doi:10.1002/mrm.22928
66. Helms G, Hagberg GE. In vivo quantification of the bound pool T1 in human white matter using the binary spin-bath model of progressive magnetization transfer saturation. *Phys Med Biol.* 2009;54:N529-N540. doi:10.1088/0031-9155/54/23/N01
67. Assländer J, Mao A, Beck ES, et al. On multi-path longitudinal spin relaxation in brain tissue. *arXiv:2301.08394v1.* 2023.
68. Zur Y, Wood ML, Neuringer LJ. Spoiling of transverse magnetization in steady-state sequences. *Magn Reson Med.* 1991;21:251-263. doi:10.1002/mrm.1910210210
69. Preibisch C, Deichmann R. Influence of RF spoiling on the stability and accuracy of T1 mapping based on spoiled FLASH with varying flip angles. *Magn Reson Med.* 2009;61:125-135. doi:10.1002/mrm.21776
70. Corbin N, Callaghan MF. Imperfect spoiling in variable flip angle T1 mapping at 7T: quantifying and minimizing impact. *Magn Reson Med.* 2021;86:693-708. doi:10.1002/mrm.28720
71. Ganter C. Steady state of gradient echo sequences with radiofrequency phase cycling: analytical solution, contrast enhancement with partial spoiling. *Magn Reson Med.* 2006;55:98-107. doi:10.1002/mrm.20736
72. Weigel M. Extended phase graphs: dephasing, RF pulses, and echoes—pure and simple. *J Magn Reson Imaging.* 2015;41:266-295. doi:10.1002/jmri.24619
73. Lustig M, Donoho DL, Santos JM, Pauly JM. Compressed sensing MRI. *IEEE Signal Process Mag.* 2008;25:72-82. doi:10.1109/MSP.2007.914728
74. Marques JP, Kober T, Krueger G, van der Zwaag W, Van de Moortele P-F, Gruetter R. MP2RAGE, a self bias-field corrected sequence for improved segmentation and T1-mapping at high field. *Neuroimage.* 2010;49:1271-1281. doi:10.1016/j.neuroimage.2009.10.002
75. Rioux JA, Levesque IR, Rutt BK. Biexponential longitudinal relaxation in white matter: characterization and impact on T1 mapping with IR-FSE and MP2RAGE. *Magn Reson Med.* 2016;75:2265-2277. doi:10.1002/mrm.25729

## SUPPORTING INFORMATION

Additional supporting information may be found in the online version of the article at the publisher's website.

**Figure S1.** Representative axial views of the difference between single-offset frequency saturation (SOFS)-normalized and dual-offset frequency saturation (DOFS)-normalized magnetization transfer (MT) images ( $\Delta = 2$  kHz and  $B_{1,RMS}^{SAT} = 3.73$   $\mu$ T) corresponding to inhomogeneous magnetization transfer ratio (ihMTR; calculated as  $ihMTR = 2 \times [MTw^{SOFS} - MTw^{DOFS}]/MT_0$ ).

**Figure S2.** Exemplary axial views of test (A,C) and retest (B,D) of macromolecular proton fraction (MPF) (A, B) and  $T_1$  (C,D) maps from the DOFS-on-resonance saturation (ONRS) framework (DOFS-MT-weighted [MTw] data and quantitative MT [qMT]-ONRS model).

**Figure S3.** Normalized histograms of voxels across the brain parenchyma of R (bin size =  $0.5$  s $^{-1}$ ) (A),  $R_1, T_{2,f}$  (bin size = 0.0005) (B),  $T_{2,b}$  (bin size =  $0.1$   $\mu$ s) (C), and MPF (bin size = 0.25%) (D). The median values of each distribution are provided.

**Figure S4.** Deviations ( $\delta$ ) as a function of  $\Delta$  and  $B_{1,RMS}^{SAT}$  of  $T_1$  (A) and MPF (B) between values estimated in the whole-brain parenchyma from qMT-ONRS analyses performed on the DOFS full Z-spectra (DOFS-ONRS framework) and values estimated from single pairs  $\{\Delta/B_{1,RMS}^{SAT}\}$  of DOFS MTw-normalized images with R,  $R_1, T_{2,f}$ , and  $T_{2,b}$  fixed to  $21.1$  s $^{-1}$ ,  $0.0158$  and  $10.0$   $\mu$ s, respectively (Figure S3).

**Figure S5.** Relative variations ( $RV_p$ ) between reference qMT parameters ( $p = \{R, T_{2,f}, T_{2,b}\}$ ) in white matter (WM; A) and gray matter (GM; B) and those estimated from synthetic data with dipolar order coupling and fitted using the qMT without considering ONRS effects (noONRS) model (SOFS-noONRS) and qMT-ONRS model (SOFS-ONRS), and from synthetic data without dipolar order coupling and fitted with the qMT-ONRS model (DOFS-ONRS).  $RV_p$ s are plotted as a function of  $T_{1D}$  for the following reference WM/GM qMT parameters:  $T_{2,f} = 20/30$  ms,  $T_{2,b} = 11/10$   $\mu$ s,  $T_1 = 1100/1600$  ms, MPF = 15/9%, and  $R = 20/20$  s $^{-1}$ . Dashed vertical gray lines refer to  $T_{1D}$  values estimated in WM ( $T_{1D} = 6.0$  ms; A) and GM ( $T_{1D} = 5.8$  ms; B), respectively.<sup>32</sup>

**Figure S6.** Bland-Altman and linear regression plots of R comparing SOFS-noONRS and DOFS-ONRS frameworks (A,B) and SOFS-ONRS and DOFS-ONRS frameworks (C,D). Bias and limits of agreements (LOAs) are indicated in dashed and solid lines, respectively, in Bland-Altman plots. Biases and LOAs of WM and DGM are reported independently, whereas the reported slopes and intercepts of the linear regression are calculated from the joint distributions (unity and regression lines are represented in full

and dashed lines, respectively). Each subject is depicted by a different symbol (circle, diamond, and square). (A) SOFS-noONRS. (B) SOFS-ONRS. (C) DOFS-ONRS.

**Figure S7.** Bland-Altman and linear regression plots of  $T_{2,f}$  comparing SOFS-noONRS and DOFS-ONRS frameworks (A,B), and SOFS-ONRS and DOFS-ONRS frameworks (C,D). Bias and LOAs are indicated in dashed and solid lines, respectively, in Bland-Altman plots. Biases and LOAs of WM and deep gray matter (DGM) are reported independently, whereas the reported slopes and intercepts of the linear regression are calculated from the joint distributions (unity and regression lines are represented in full and dashed lines, respectively). Each subject is depicted by a different symbol (circle, diamond, and square). (A) SOFS-noONRS. (B) SOFS-ONRS. (C) DOFS-ONRS.

**Figure S8.** Bland-Altman and linear regression plots of  $T_{2,b}$  comparing SOFS-noONRS and DOFS-ONRS frameworks (A,B) and SOFS-ONRS and DOFS-ONRS frameworks (C,D). Bias and LOAs are indicated in dashed and solid lines, respectively, in Bland-Altman plots. Biases and LOAs of WM and DGM are reported independently, whereas the reported slopes and intercepts of the linear regression are calculated from the joint distributions (unity and regression lines are represented in full and dashed lines, respectively). Each subject is depicted by a different symbol (circle, diamond, and square). (A) SOFS-noONRS. (B) SOFS-ONRS. (C) DOFS-ONRS.

**Table S1.** Summary of qMT-derived average values for R,  $T_{2,f}$ , and  $T_{2,b}$  in WM and DGM of the fits for qMT-noONRS applied to SOFS-MTw data (SOFS-noONRS), qMT-ONRS model applied to SOFS-MTw data (SOFS-ONRS), and the qMT-ONRS model applied to DOFS-MTw data (DOFS-ONRS).

**Table S2.** Summary of qMT parameters of the reproducibility experiment estimated by the DOFS-ONRS framework and evaluated by Bland-Altman and linear regression analyses. The coefficient of variation between test and retest experiments is provided.

**How to cite this article:** Soustelle L, Troalen T, Hertanu A, et al. Quantitative magnetization transfer MRI unbiased by on-resonance saturation and dipolar order contributions. *Magn Reson Med.* 2023;1-19. doi: 10.1002/mrm.29678

## APPENDIX A

### A.1 Equations with dipolar order

The objective is to isolate the longitudinal magnetization of the free pool ( $M_{z,f}$ ) from the magnetization vector  $\mathbf{M}' = [M_{x,f} \ M_{y,f} \ M_{z,f} \ M_{z,b} \ \beta]^T$ , where  $\beta$  is related to

the dipolar order (characterized by  $T_{1D}$ ) coupled with the macromolecular Zeeman order.

The general cross-relaxation matrix ( $\mathbf{A}'_{\text{REX}}$ ) derived from Eq. (4) becomes

$$\mathbf{A}'_{\text{REX}} = \begin{bmatrix} -1/T_{2f} & 0 & 0 & 0 & 0 \\ 0 & -1/T_{2f} & 0 & 0 & 0 \\ 0 & 0 & -(R_{1f} + RM_{0,b}) & RM_{0,f} & 0 \\ 0 & 0 & RM_{0,b} & -(R_{1,b} + RM_{0,f}) & 0 \\ 0 & 0 & 0 & 0 & -1/T_{1D} \end{bmatrix} \quad (\text{A1})$$

The saturation matrix ( $\mathbf{A}'_{\text{SAT}}$ ) associated with the MT preparation pulse is now defined as

$$\mathbf{A}'_{\text{SAT}} = \begin{bmatrix} 0 & 0 & 0 & 0 & 0 \\ 0 & 0 & 0 & 0 & 0 \\ 0 & 0 & -W_f^{\text{SAT}} & 0 & 0 \\ 0 & 0 & 0 & -W_b^{\text{SAT}} & W_b^{\text{SAT}} 2\pi\Delta \\ 0 & 0 & 0 & W_b^{\text{SAT}} 2\pi\Delta/D^2 & -W_b^{\text{SAT}} (2\pi\Delta/D)^2 \end{bmatrix} \quad (\text{A2})$$

where  $D$  is the local dipolar field expressed in angular frequency unit, which may be calculated from the second moment of  $g_b(\Delta, T_{2,b})$  or alternatively as  $1/(T_{2,b}\sqrt{15})$  for the super-Lorentzian lineshape model.

$\mathbf{A}_{\text{RO}}$  is simply augmented into  $\mathbf{A}'_{\text{RO}}$  to match dimensionality, because no dipolar order is generated for on-resonance saturation:

$$\mathbf{A}'_{\text{RO}} = \begin{bmatrix} \mathbf{A}_{\text{RO}} \\ 0 \end{bmatrix} \quad (\text{A3})$$

$\tilde{\mathbf{A}}_i$  matrices (Eq. [7]) are rewritten by substituting  $\mathbf{A}_i$  with  $\mathbf{A}'_i$ ,  $\mathbf{C}$  with  $\mathbf{C}' = [0 \ 0 \ R_{1,f}M_{0,f} \ R_{1,b}M_{0,b} \ 0]^T$ , and matching the dimensionality of the “0” lower row vector. Finally, Eq. (8) is used to calculate the steady-state vector of interest.